Science operation plan of Phobos and Deimos from the MMX spacecraft

Tomoki Nakamura, Hitoshi Ikeda, Toru Kouyama, Hiromu Nakagawa, Hiroki Kusano, Hiroki Senshu, Shingo Kameda, Koji Matsumoto, Ferran Gonzalez-Franquesa, Naoya Ozaki, et al.

HAL Id: obspm-03600677
https://hal-obspm.ccsd.cnrs.fr/obspm-03600677v1

Submitted on 8 Mar 2022

Earth, Planets and Space

FULL PAPER

Science operation plan of Phobos and Deimos from the MMX spacecraft

Tomoki Nakamura[1*], Hitoshi Ikeda[2], Toru Kouyama[3], Hiromu Nakagawa[1], Hiroki Kusano[4], Hiroki Senshu[5], Shingo Kameda[6], Koji Matsumoto[7,8], Ferran Gonzalez-Franquesa[8], Naoya Ozaki[9], Yosuke Takeo[2], Nicola Baresi[10], Yusuke Oki[2], David J. Lawrence[11], Nancy L. Chabot[11], Patrick N. Peplowski[11], Maria Antonietta Barucci[12], Eric Sawyer[13], Shoichiro Yokota[14], Naoki Terada[1], Stephan Ulamec[15], Patrick Michel[16], Masanori Kobayashi[5], Sho Sasaki[14], Naru Hirata[17], Koji Wada[5], Hideaki Miyamoto[18], Takeshi Imamura[18], Naoko Ogawa[19], Kazunori Ogawa[19], Takahiro Iwata[9], Takane Imada[19], Hisashi Otake[19], Elisabet Canalias[13], Laurence Lorda[13], Simon Tardivel[13], Stéphane Mary[13], Makoto Kunugi[20], Seiji Mitsuhashi[21], Alain Doressoundiram[12], Frédéric Merlin[12], Sonia Fornasier[12], Jean-Michel Reess[12], Pernelle Bernardi[12], Shigeru Imai[22], Yasuyuki Ito[22], Hatsumi Ishida[22], Kiyoshi Kuramoto[23] and Yasuhiro Kawakatsu[9]

Abstract

The science operations of the spacecraft and remote sensing instruments for the Martian Moon eXploration (MMX) mission are discussed by the mission operation working team. In this paper, we describe the Phobos observations during the first 1.5 years of the spacecraft's stay around Mars, and the Deimos observations before leaving the Martian system. In the Phobos observation, the spacecraft will be placed in low-altitude quasi-satellite orbits on the equatorial plane of Phobos and will make high-resolution topographic and spectroscopic observations of the Phobos surface from five different altitudes orbits. The spacecraft will also attempt to observe polar regions of Phobos from a three-dimensional quasi-satellite orbit moving out of the equatorial plane of Phobos. From these observations, we will constrain the origin of Phobos and Deimos and select places for landing site candidates for sample collection. For the Deimos observations, the spacecraft will be injected into two resonant orbits and will perform many flybys to observe the surface of Deimos over as large an area as possible.

Keywords: MMX mission, Phobos, Deimos, QSO, Flyby

*Correspondence: tomoki.nakamura.a8@tohoku.ac.jp
[1] Tohoku University, Sendai, Japan
Full list of author information is available at the end of the article

Nakamura *et al. Earth, Planets and Space* (2021) 73:227

Page 2 of 27

Graphical Abstract

Science operation plan of Phobos and Deimos from the MMX spacecraft

Strategy for close-up observation of Phobos from low-altitude quasi-satellite orbits

Wide coverage of Deimos by multiple flyby observation using resonant orbitsc
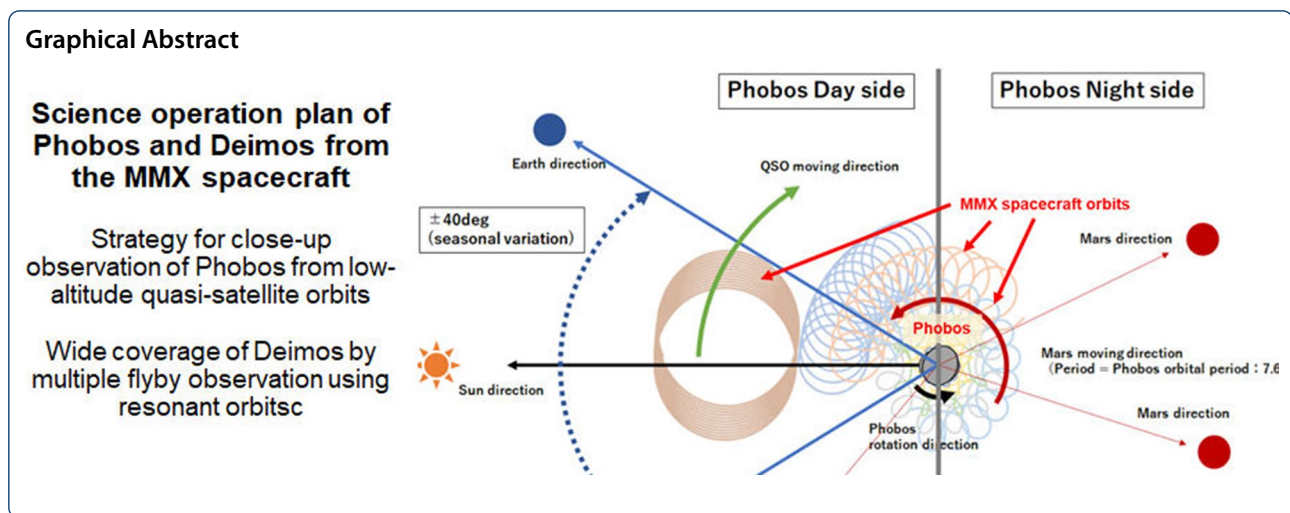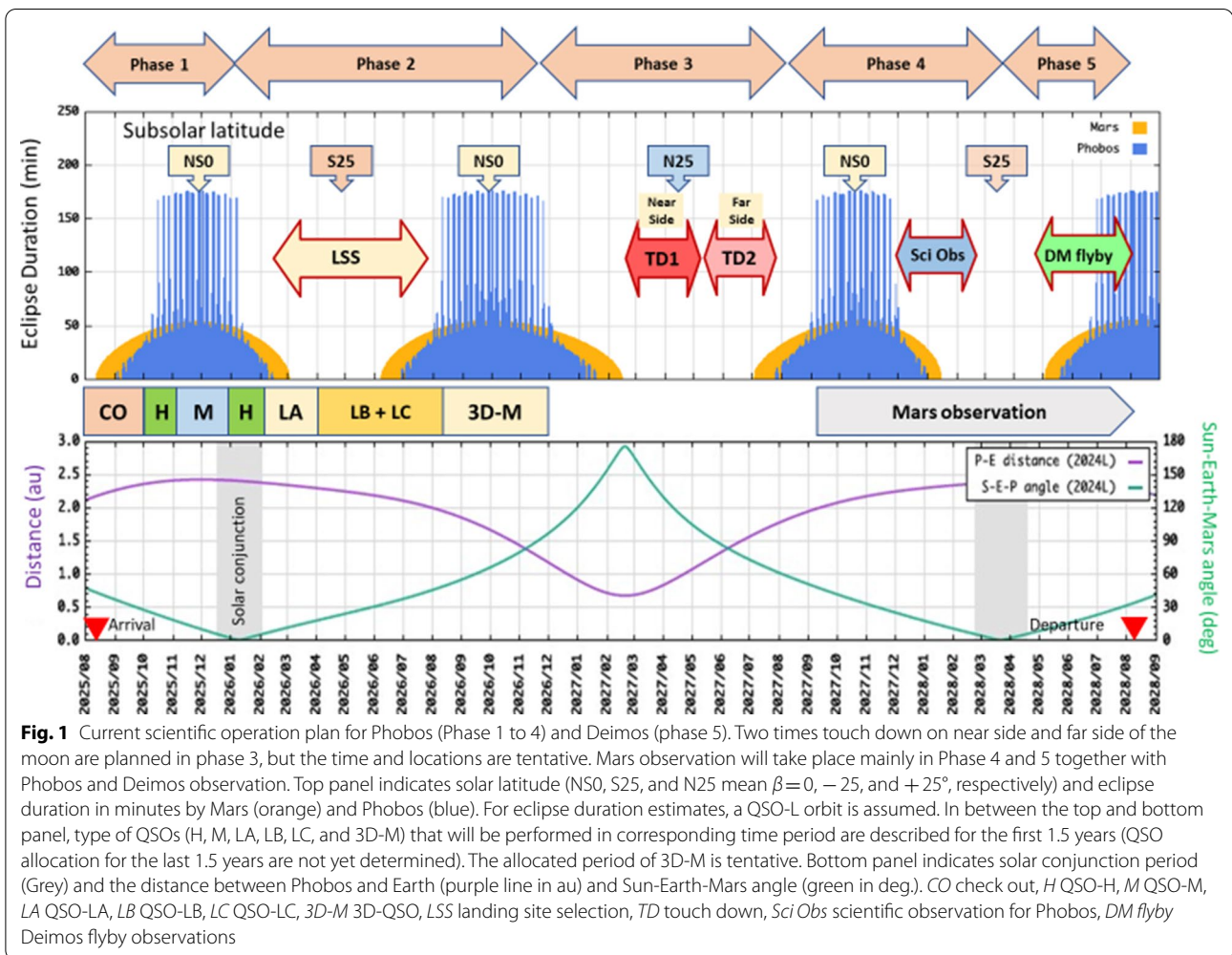
Introduction

The Martian Moon eXploration (MMX) mission aims to return samples from Phobos, one of the Martian satellites, and is now being developed by the MMX project team organized by JAXA (Kuramoto et al. 2021). This mission is the third sample return mission by Japan, following Hayabusa (Fujiwara et al. 2006; Nakamura et al. 2011) and Hayabusa2 (Watanabe et al. 2019) missions. The goal of the mission is to clarify the origin of Phobos and Deimos. Through the formation process of the Martian moons, we can understand the formation process of the satellite systems of the inner planets and, if the moons formed by capture of primitive asteroids (Burns 1978) or a giant impact (Craddock 2011), the nature of the small bodies that flew from the outer to the inner solar system. The MMX mission is designed to fulfill all mission objectives and the mission requirements including operation requirements for instruments are detailed in Kuramoto et al. (2021).

The spacecraft will be launched in 2024, inserted into Mars orbit in 2025, and stay in the Martian area for about 3 years. It will perform scientific observations of Phobos from low altitudes and select sample collection sites. The spacecraft will then land on the surface of Phobos, collect samples, and return to Earth in 2029. Before entering the orbit to return to Earth, the spacecraft will carry out a flyby observation of Deimos, the other Martian satellite. There have been many space missions to Mars, and several spacecraft are still orbiting Mars for observation such as Mars Express (Witasse et al. 2014). Some spacecrafts observed Phobos and Deimos as a secondary objective (Duxbury et al. 2014). On the other hand, only a few missions have tried to observe Phobos as a main target, such as Phobos-1 and Phobos-2 in 1988 (Sagdeev and Zakharov 1989) and Phobos-Grunt in 2011 (Marov et al. 2004), but none of the missions were fully successful. Therefore, the MMX mission is definitely different from the previous missions in that it will mainly observe the Martian satellites and will also collect and bring back samples to Earth.

The major difference of MMX from the preceding Hayabusa and Hayabusa2 missions is that, unlike asteroids that exist in interplanetary space as stand-alone objects, the Martian moons orbit Mars, under the influence of Mars' gravity. Therefore, to observe the Martian moons, the spacecraft must orbit Mars in the same way as the Martian moons. In addition, the target bodies of Hayabusa and Hayabusa2, Itokawa and Ryugu, respectively, were small bodies with a diameter of less than 1 km, while the target bodies of MMX, Phobos and Deimos, are larger than 10 km. Therefore, when conducting close observations of Phobos, it is necessary to put the spacecraft into an orbit going around Phobos to obtain centrifugal force to counteract the gravitational force and, therefore, cannot easily hover or stay at a Home Position, as Hayabusa and Hayabusa2 did (Watanabe et al. 2019). Thus, close observations of the Martian moons require consideration of the gravitational effects of both Mars and the Martian moons, which is critically different from the observations of small asteroids.

In this paper, we describe science operations for the close-up observation of Phobos and the flyby observation of Deimos. As mentioned above, it is unprecedented to observe the Martian moons for a long period of time, and thus it is important to describe properly how to establish the operation policies of the spacecraft and how to plan spacecraft orbits and corresponding scientific observations. We hope that this paper will serve as a guide when planning long-term observations of small satellites around large planets in the future.

Nakamura *et al. Earth, Planets and Space* (2021) 73:227

Page 3 of 27

Fig. 1 Current scientific operation plan for Phobos (Phase 1 to 4) and Deimos (phase 5). Two times touch down on near side and far side of the moon are planned in phase 3, but the time and locations are tentative. Mars observation will take place mainly in Phase 4 and 5 together with Phobos and Deimos observation. Top panel indicates solar latitude (NS0, S25, and N25 mean $\beta = 0$, -25, and $+25°$, respectively) and eclipse duration in minutes by Mars (orange) and Phobos (blue). For eclipse duration estimates, a QSO-L orbit is assumed. In between the top and bottom panel, type of QSOs (H, M, LA, LB, LC, and 3D-M) that will be performed in corresponding time period are described for the first 1.5 years (QSO allocation for the last 1.5 years are not yet determined). The allocated period of 3D-M is tentative. Bottom panel indicates solar conjunction period (Grey) and the distance between Phobos and Earth (purple line in au) and Sun-Earth-Mars angle (green in deg.). *CO* check out, *H* QSO-H, *M* QSO-M, *LA* QSO-LA, *LB* QSO-LB, *LC* QSO-LC, *3D-M* 3D-QSO, *LSS* landing site selection, *TD* touch down, *Sci Obs* scientific observation for Phobos, *DM flyby* Deimos flyby observations
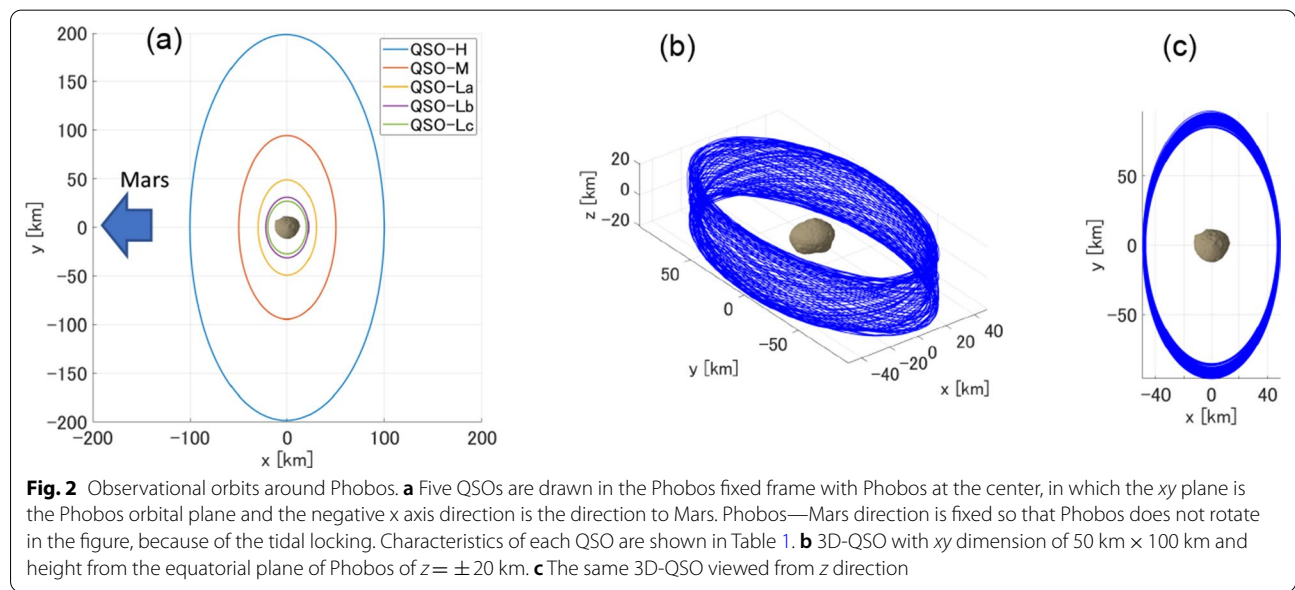
Overall scientific operation and observation plan

The spacecraft will stay around Mars for 3 years, from September 2025 to September 2028. Figure 1 shows the overall operation plan of the spacecraft for 3 years. Five science observation phases are defined in consideration of important operational events and arrangement of Phobos, Mars, and Earth. Phase 1: initial check-out of instruments and initial observation of Phobos; Phase 2: phobos proximity observation to select landing sites; Phase 3: two landings on Phobos and rover delivery to Phobos; Phase 4: science observations of Phobos and Mars; Phase 5: science observations of Deimos and Mars. The reason for landing in Phase 3 is that the Earth-Phobos distance is minimum (shortest communication time) and the Sun-Phobos distance is maximum (lowest Phobos surface temperature: Fig. 1 bottom) in this phase. The reason why the observation of Deimos was set in Phase 5 is that when putting the spacecraft into the Earth return orbit, it is necessary to

gradually expand the orbital radius starting from the Phobos orbit, and thus a good opportunity to observe Deimos will come on the way.

Solar conjunctions will occur in January 2026 and March 2028 during the 3-year stay around Mars (Fig. 1 bottom). For about a month around the conjunction, the Sun-Earth-Phobos angle will be less than a few degrees (Fig. 1 bottom), making communication with Earth difficult. Therefore, the spacecraft will be placed into a higher altitude to escape the eclipses during this period. In addition, Mars will reach the equinox in November 2025, and then reach equinoxes in every half-year (about 11 months) cycle of Mars. Before and after equinoxes, the spacecraft will be in the shade behind Mars and Phobos (eclipses), because it orbits near the equatorial plane of Mars (see "Observation orbits from the vicinity of Phobos" section for details). In addition, since the direction of the rotation axis of Mars is almost coincident with that of Phobos, the position of the Sun as seen from Phobos (solar latitude) becomes equatorial (0 latitude) at the time

Nakamura *et al. Earth, Planets and Space*   (2021) 73:227

Page 4 of 27

Table 1 QSO characteristics

QSO	Size	Period (Phobos fixed)	Period (inertial frame)	Day/night side duration time	Polar angle at min distance (°)	Polar angle at max distance (°)
QSO-H	100 km × 198 km	7.59 h	32 days	16 day	10	5
QSO-M	50 km × 94 km	7.13 h	4.3 days	2.1 days	21	11
QSO-LA	30 km × 49 km	5.76 h	24.3 h	12 h	35	21
QSO-LB	22 km × 31 km	4.40 h	11.5 h	5.8 h	50	33
QSO-LC	20 km × 27 km	3.97 h	9.3 h	4.7 h	54	39

Fig. 2 Observational orbits around Phobos. **a** Five QSOs are drawn in the Phobos fixed frame with Phobos at the center, in which the *xy* plane is the Phobos orbital plane and the negative x axis direction is the direction to Mars. Phobos—Mars direction is fixed so that Phobos does not rotate in the figure, because of the tidal locking. Characteristics of each QSO are shown in Table 1. **b** 3D-QSO with *xy* dimension of 50 km × 100 km and height from the equatorial plane of Phobos of $z = \pm 20$ km. **c** The same 3D-QSO viewed from z direction

of the Martian equinoxes. The solar latitude then moves up to 25° to the southern or northern hemisphere side between equinoxes (Fig. 1 top). We define here the solar latitude (β angle) to describe the position of the Sun: if the Sun is the zenith of northern or southern hemisphere, then $\beta > 0$ or $\beta < 0$, respectively. If the Sun is the zenith of the equator, then $\beta = 0$.

Some instruments require sun illumination on the observed areas to acquire clear images and good signal/noise spectra, and consequently the sun elevation on Phobos (β angle) has a major impact on planning observations. Low absolute values of β angle, i.e., close to 0, are favorable for the observation of both northern and southern hemispheres, while high absolute values ($\beta > 0$ or $\beta < 0$) favor the observation of only one hemisphere but restrains the possibility to observe the pole areas of the other hemisphere. The first Phobos observation from October 2025 in phase1 will be performed from orbits with low absolute values of β angle, which is ideal to get a global mapping of both hemispheres. On the other hand, during low altitude orbits in phase 2, the absolute values

of β angle will be very high, which is ideal for observation of the southern hemisphere but induces low sun elevation for observation of the northern hemisphere.

In this paper, we describe the Phobos observations operated in Phases 1 and 2, and the Deimos observations in Phase 5. The observation plan for Phases 3 and 4 is currently under consideration and will be completed within 1 year. Mars observations are described in the companion paper (Ogohara et al. 2021).

## Observation orbits from the vicinity of Phobos

For Phobos observation, the spacecraft will orbit around Mars like a Martian moon and trace out periodic retrograde ellipses around Phobos known as quasi-satellite orbits (QSO). The plan includes five QSO orbits with different altitudes from Phobos, defined as QSO-H, -M, -LA, -LB, and -LC in decreasing order of altitude. The characteristics of each of the five candidate QSOs is tabulated in Table 1 and Fig. 2a (details of the QSOs for the MMX mission are described in Baresi et al. 2020; Pushparaj et al. 2021; Chikazawa et al. 2021). In all five

Nakamura *et al. Earth, Planets and Space* (2021) 73:227

Page 5 of 27

of the QSOs, the spacecraft orbits in the equatorial plane of Phobos. The lower the altitude of the spacecraft, the greater the gravitational influence of Phobos. Therefore, at the lower the altitude of the QSO, the orbital period of the spacecraft around Phobos becomes shorter, and at the same time, the speed of the spacecraft relative to Phobos' surface becomes faster (Table 1). The orbital period gives an indication of the necessary time to perform a full longitudinal coverage for global mapping.
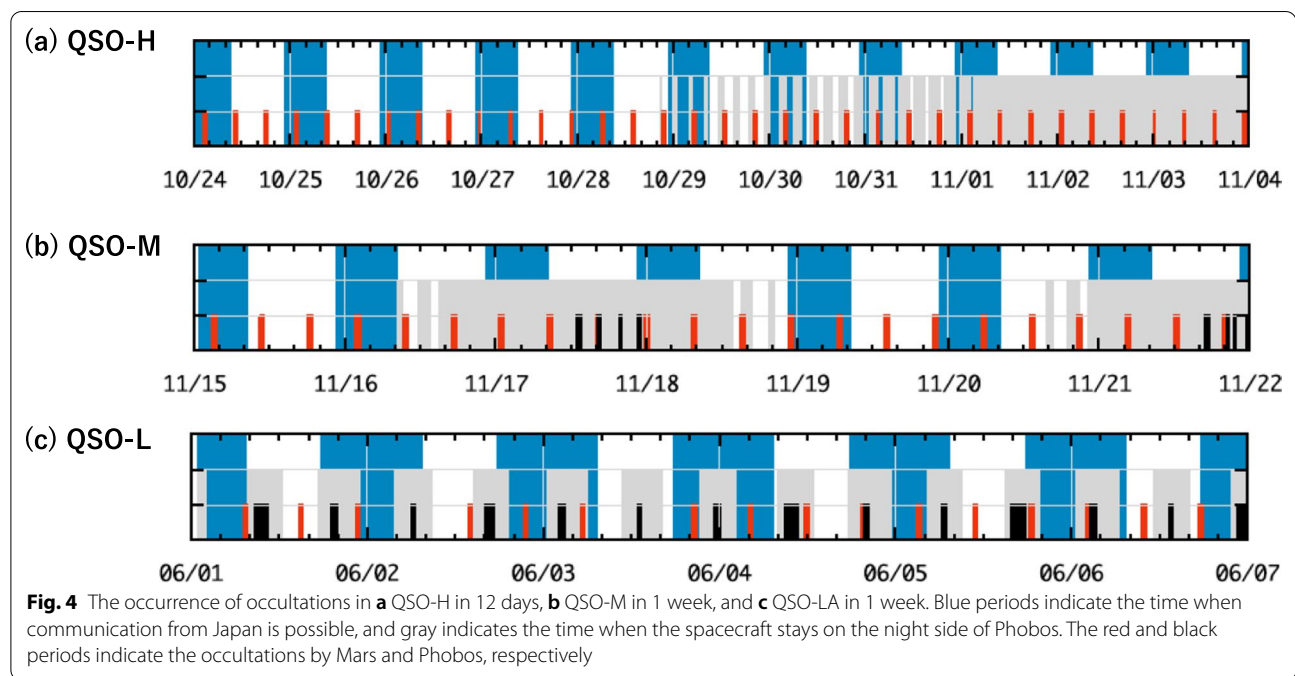
Figure 2 shows different QSOs in a rotating reference frame centered on Phobos and such that the *x*-axis is constantly aligned with the Mars-Phobos direction. It follows that the direction of Mars is to the left of this figure. In addition, the Martian moons, like the Earth's moon, always face the same direction to Mars (a phenomenon called tidal locking). Therefore, in Fig. 2, where the Mars direction is fixed, Phobos does not rotate. All QSOs are elliptical: on the Martian and anti-Martian sides of Phobos, the altitude of the spacecraft is minimized and the ground speed is maximized at the same time. Therefore, at the same QSO, the sub-Mars and the anti-Mars side can be observed and characterized at higher resolution.

On the other hand, the closer the spacecraft comes to Phobos, the higher is the viewing incidence angle on high latitude areas. Consequently, polar observations are not possible from equatorial low altitude QSOs and reachable latitudes decrease when the spacecraft comes closer. Phobos polar angles with the altitude are shown in Table 1. For instruments with a narrow field of view, latitudinal mapping is realized by cross-track offsets of the spacecraft attitude with respect to the Phobocentric pointing. To observe the polar regions with lower polar angles, the spacecraft must move north or south from the equatorial plane of Phobos. For this purpose, the QSO-M orbit is gradually tilted to be oblique to the equatorial plane of Phobos. Figure 2b, c show the orbits obtained in this way (hereafter called 3D-QSO). Using this orbit, we can observe the polar region with high resolution and refine the shape model of the Phobos. The timing and period of the 3D-QSO observation is tentatively allocated in the second eclipse period (Fig. 1 top) because 3D-QSO can largely escape the eclipse effects.

Figure 3 illustrates the same QSOs orbits in an inertial coordinate system centered on Phobos. Here, sun is located on the left side, indicating that the left side of Phobos corresponds to the day side. Contrary to the illustration in Fig. 2, Phobos rotates at the center of Fig. 3. Using these diagrams, we can tell at a glance whether the spacecraft is on the day side or the night side of Phobos. Many instruments will observe only the day side of the Phobos, and thus this diagram will make it easier to plan
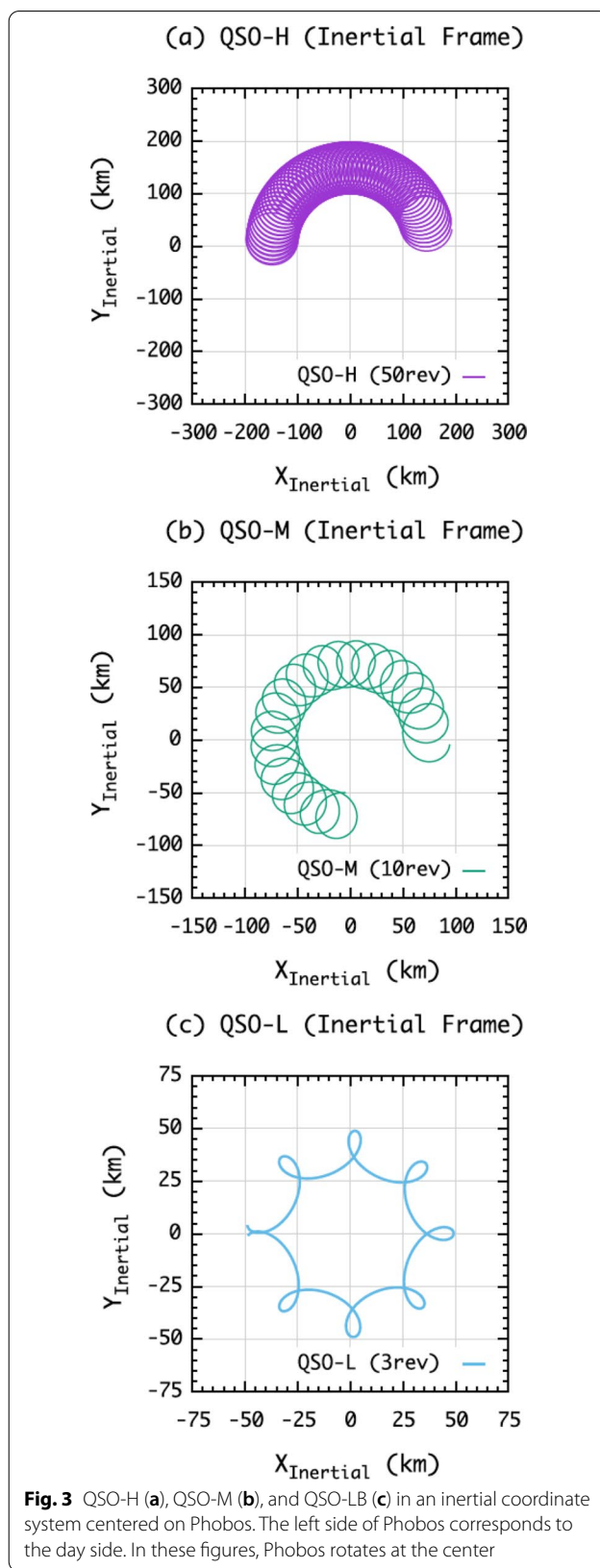
Fig. 3 QSO-H (**a**), QSO-M (**b**), and QSO-LB (**c**) in an inertial coordinate system centered on Phobos. The left side of Phobos corresponds to the day side. In these figures, Phobos rotates at the center

Fig. 4 The occurrence of occultations in **a** QSO-H in 12 days, **b** QSO-M in 1 week, and **c** QSO-LA in 1 week. Blue periods indicate the time when communication from Japan is possible, and gray indicates the time when the spacecraft stays on the night side of Phobos. The red and black periods indicate the occultations by Mars and Phobos, respectively
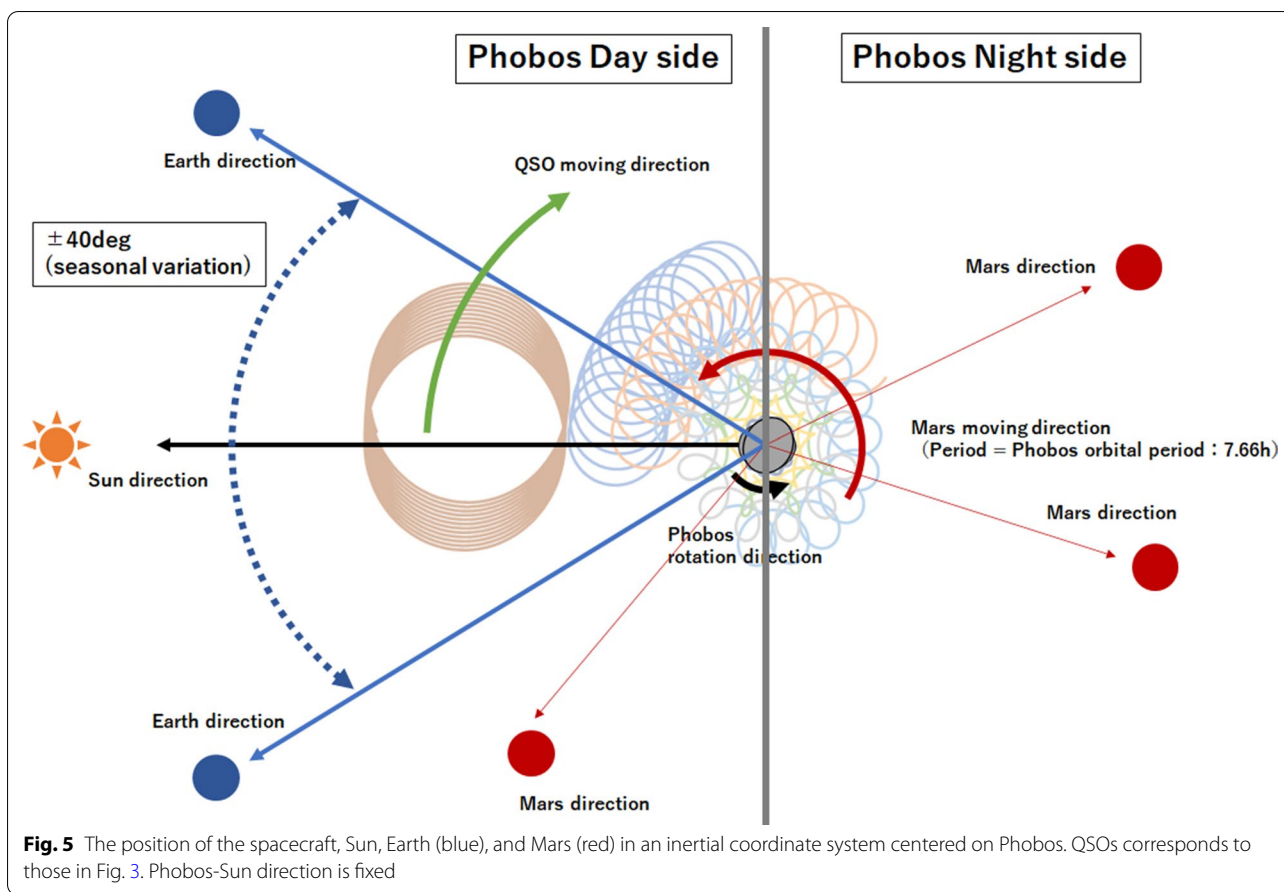
the scientific observations. For example, in the case of QSO-H, the spacecraft will stay on the day side of Phobos for 16 days before moving to the night side of the Phobos and will remain in the night side of Phobos for another 16 days (Fig. 3a and Table 1). It follows that the observation at QSO-H must be concentrated on the 16 days on the day side. The period of the spacecraft's day/night cycle differs from orbit to orbit depending on the altitude of MMX (Table 1). The lower the altitude, the shorter the day/night cycle.

One of the characteristic geometric conditions that should be considered when observing from the vicinity of Phobos is eclipses by Mars and Phobos. During these eclipses, the spacecraft will stay in the shadow behind Mars or Phobos. Long eclipse periods reduce the power generation of the spacecraft's solar panels, which has a significant impact on the spacecraft's operation. Therefore, long eclipse periods must be avoided. The duration of a single eclipse by Mars is less than 1 h, but the duration of the eclipse by Phobos depends on the orbital shape in the inertial coordinate system (vertical scale of Fig. 1 top), and it varies depending on the periods that the spacecraft stays in the Phobos shadow areas (Chikazawa et al. 2021). Particularly, during the low altitude operations, the long duration of eclipse (more than 10,000 s) occurs when the inner cycloidal shaped circle overlaps with the shadowed areas (Fig. 3). The circles correspond to the regions of slow relative velocity located

at the leading side and trailing side in the Phobos fixed coordinate system. To minimize the effect of the eclipse by Mars and Phobos, it is necessary to make an observation plan to avoid the low altitude operation (QSO-LA, -LB, and -LC) in the season when the long eclipses occur.

In addition to eclipse, another geometric condition to consider is occultation. During this period, the spacecraft is not visible from the Earth because it is blocked by Mars or Phobos, thus limiting the communications between the Earth and the spacecraft. Figure 4 shows the occurrence of occultations in some QSOs. In the figure, the red and black periods indicate the occultation by Mars and Phobos, respectively. It can be seen that both Mars and Phobos occultations occur frequently in lower altitude orbits (Fig. 4). As described above, unlike asteroid observations, Martian moon observations have many additional constraints to be considered when optimizing scientific observations.

Figure 5 shows the position of the spacecraft relative to the Sun, Earth, and Mars centered on Phobos. In the actual observation of Phobos from the QSO, only the day side of Phobos is observed except for some instruments such as MEGANE. On the other hand, the spacecraft needs to be oriented to the Earth periodically to transmit scientific data and spacecraft telemetry information. The direction of the Earth varies within a range of ±40° relative to the solar direction during the spacecraft's QSO stay. It is also desirable to observe Mars in

Nakamura *et al. Earth, Planets and Space* (2021) 73:227

Page 7 of 27

Fig. 5 The position of the spacecraft, Sun, Earth (blue), and Mars (red) in an inertial coordinate system centered on Phobos. QSOs corresponds to those in Fig. 3. Phobos-Sun direction is fixed

Table 2 MMX remote sensing apparatus

	G-, N-ray spectrometer	Visible camera	Multi (7)-band camera	LIDAR	Near-infrared spectrometer	Mass spectroemter	Dust counter
Name	MEGANE	TENGOO	OROCHI	LIDAR	MIRS	MSA	CMDM
Wavelength range	Gamma-ray: 200 keV–10 MeV (0.12–6.2 pm), neutron-ray: 20–7 MeV	0.45–0.65 μm	390 nm, 480 nm, 550 nm, 650 nm, 730 nm, 860 nm, and 950 nm	1.064 μm	0.9–3.6 μm		
FOV	γ-ray: Nadia (0°)±45°(cone), neutron-ray: 2π	~0.7°	> ~60°	0.5 mrad	3.3° × 0.35 mrad	2-pi sr	pi sr
iFOV (pixel size)		5.9 μrad	0.44–0.46 mrad		0.35 mrad		
Panel and direction of FOV	−Z panel −Z direction	−Z panel −Z direction	−Z panel −Z direction	−Z panel −Z direction	−Z panel −Z direction	−Z panel −Z direction	−X panel −X direction
Objectives	Major element composition	Surface morphology	Visible spectra	Reflectance at 1.064 μm	Hydrous minerals	Pick-up ion	Interplanetary dust
	Neutron, hydrogen	Craters	0.65 fieature	(Phase angle 0°)	Organics	Reflectance ion	Mars dust ring

between Phobos observations (especially while the spacecraft is on the night side of Phobos: Ogohara et al. 2021). Phobos rotates with a rotation period of 7.66 h, and the spacecraft orbits Phobos in the opposite direction of its rotation. As mentioned above, the time for the spacecraft to circle the day and night side of Phobos depends on the altitude of the QSO (Table 1 and Fig. 3).

Nakamura *et al. Earth, Planets and Space* (2021) 73:227

Page 8 of 27
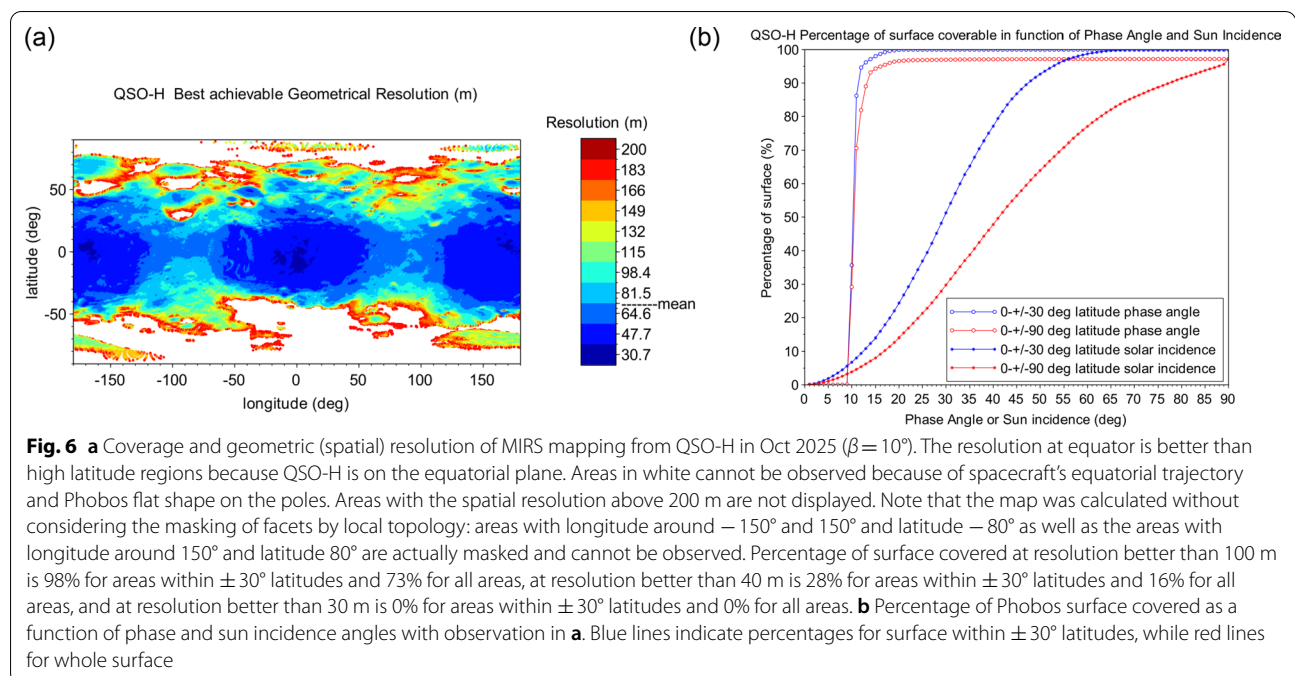
Fig. 6 **a** Coverage and geometric (spatial) resolution of MIRS mapping from QSO-H in Oct 2025 ($\beta = 10°$). The resolution at equator is better than high latitude regions because QSO-H is on the equatorial plane. Areas in white cannot be observed because of spacecraft's equatorial trajectory and Phobos flat shape on the poles. Areas with the spatial resolution above 200 m are not displayed. Note that the map was calculated without considering the masking of facets by local topology: areas with longitude around −150° and 150° and latitude −80° as well as the areas with longitude around 150° and latitude 80° are actually masked and cannot be observed. Percentage of surface covered at resolution better than 100 m is 98% for areas within ±30° latitudes and 73% for all areas, at resolution better than 40 m is 28% for areas within ±30° latitudes and 16% for all areas, and at resolution better than 30 m is 0% for areas within ±30° latitudes and 0% for all areas. **b** Percentage of Phobos surface covered as a function of phase and sun incidence angles with observation in **a**. Blue lines indicate percentages for surface within ±30° latitudes, while red lines for whole surface

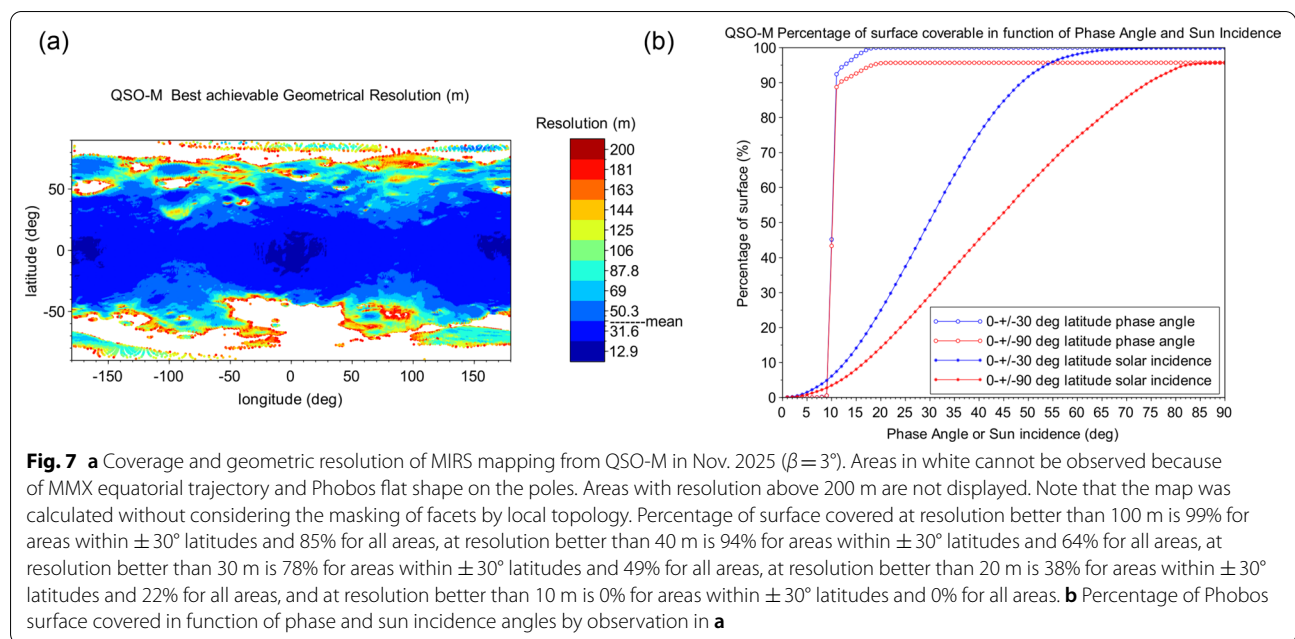## Scientific observation plan for Phobos by individual apparatus in Phase 1 and 2

We have seven major scientific instruments onboard the MMX spacecraft (Table 2). MMX near-infrared spectrometer (MIRS) equipped with a scanning mirror to follow the along-track direction of ±20° capacity will obtain reflectance spectra with a wavelength range from 0.9 to 3.6 μm to characterize surface minerals of Phobos and Deimos (Barucci et al. 2021). Observation of surface Reflectance by Optical Chromatic Imager (OROCHI) is composed of seven wide-angle bandpass imagers with center wavelengths of 390 nm, 480 nm, 550 nm, 650 nm, 730 nm, 860 nm, and 950 nm (Kameda et al. 2021), and the main objective is to acquire spectral mapping. Telescopic Nadir Imager for Geomorphology (TENGOO) is a visible telescope camera that obtains high resolution images to reveal the geomorphological feature of Phobos and Deimos (Kameda et al. 2021). Mars-moon Exploration with GAmma rays and Neutrons (MEGANE) is a gamma-ray and neutron spectrometer that measures major element composition of Phobos (Lawrence et al. 2019). Mass Spectrum Analyzer (MSA) is a mass spectrometer whose main objective is to estimate flux ratios of secondary ions from Phobos' surface sputtered by solar wind (Yokota et al. 2021). Circum-Martian Dust Monitor (CMDM) is a dust counter to detect interplanetary dust and any Mars dust ring (Kobayashi et al. 2018). Laser Imaging Detection and Ranging (LIDAR) uses a laser beam with a wavelength of 1 micron to measure

the distance between the spacecraft and Phobos and to observe the topography of the Phobos surface (Senshu et al. 2021). In the following sections, we introduce the scientific operation plans for individual instruments at different QSOs.

As for the *X*, *Y*, and *Z* panels of the spacecraft (Table 2), the $+X$ or $-X$ panel faces the direction of travel of the spacecraft in the QSO. The $+Y$ panel faces the vertical south or north direction of the QSO orbit plane when $+X$ or $-X$ panel faces moving direction, respectively. The $+Z$ plane points toward the gravitational center of the phobos in QSOs. Most of the instruments are in the $-Z$ plane and are oriented toward the phobos from the QSO. Among the major instruments, only CMDM is in the $-X$ plane, and its field of view is also in the $-X$ direction (Table 2).

MIRS
QSO-H
One of MIRS objectives is to provide a spectral mapping as global as possible to determine Phobos' surface composition and thermal inertia. Considering MIRS cross-track field-of-view of 3.3° and maximum Phobos polar angle from QSO-H of 10° (Table 1), three complete longitudinal coverages are necessary to obtain a global mapping, one with each of the cross-track angles −3°, 0°, and 3°. Settings of current QSO-H are such that Sun-Phobos-Spacecraft angle is below 90° (i.e., spacecraft is located in dayside) for the first 16 days, allowing Phobos

Fig. 7 a Coverage and geometric resolution of MIRS mapping from QSO-M in Nov. 2025 ($\beta = 3°$). Areas in white cannot be observed because of MMX equatorial trajectory and Phobos flat shape on the poles. Areas with resolution above 200 m are not displayed. Note that the map was calculated without considering the masking of facets by local topology. Percentage of surface covered at resolution better than 100 m is 99% for areas within $\pm 30°$ latitudes and 85% for all areas, at resolution better than 40 m is 94% for areas within $\pm 30°$ latitudes and 64% for all areas, at resolution better than 30 m is 78% for areas within $\pm 30°$ latitudes and 49% for all areas, at resolution better than 20 m is 38% for areas within $\pm 30°$ latitudes and 22% for all areas, and at resolution better than 10 m is 0% for areas within $\pm 30°$ latitudes and 0% for all areas. **b** Percentage of Phobos surface covered in function of phase and sun incidence angles by observation in **a**

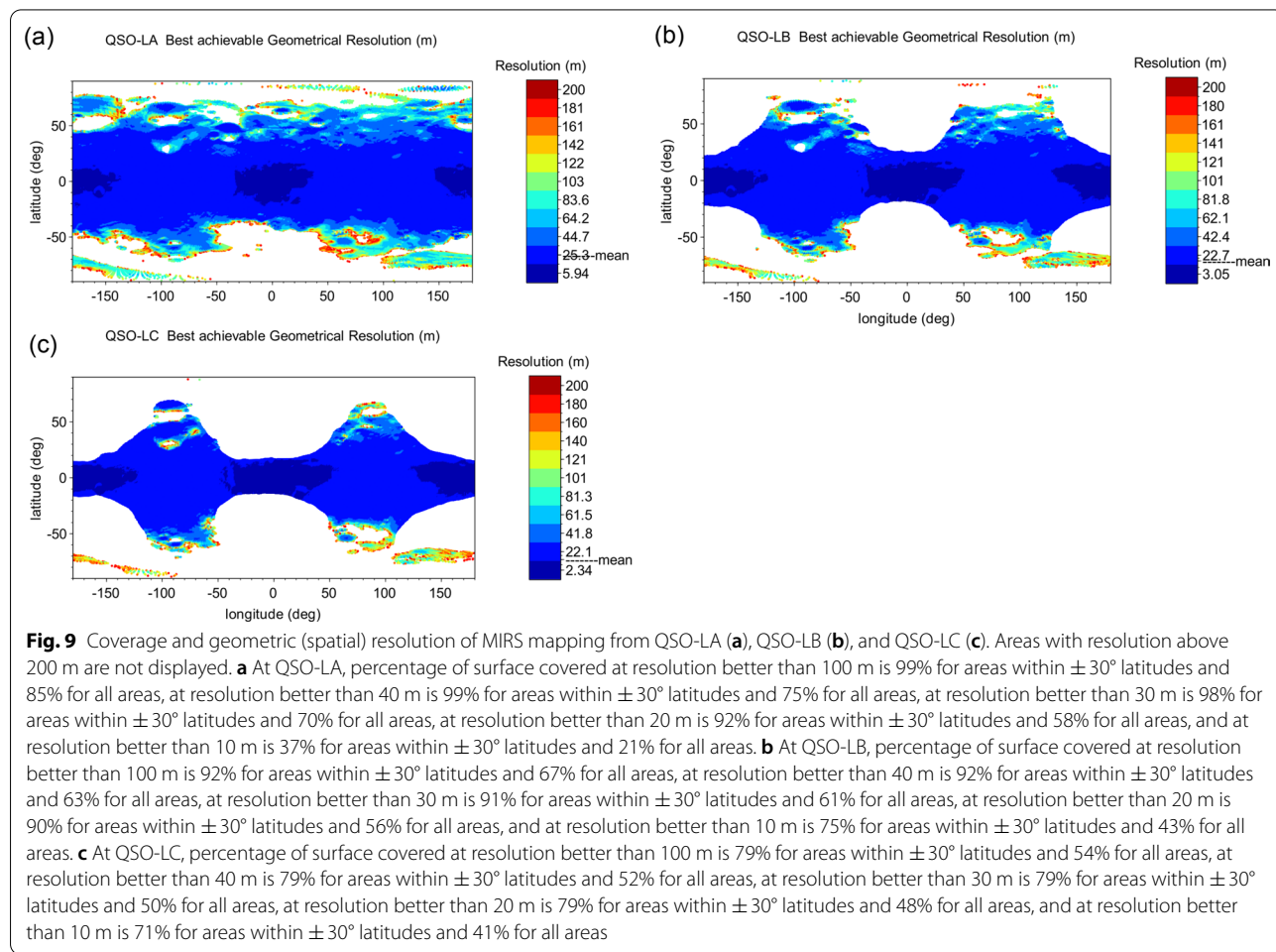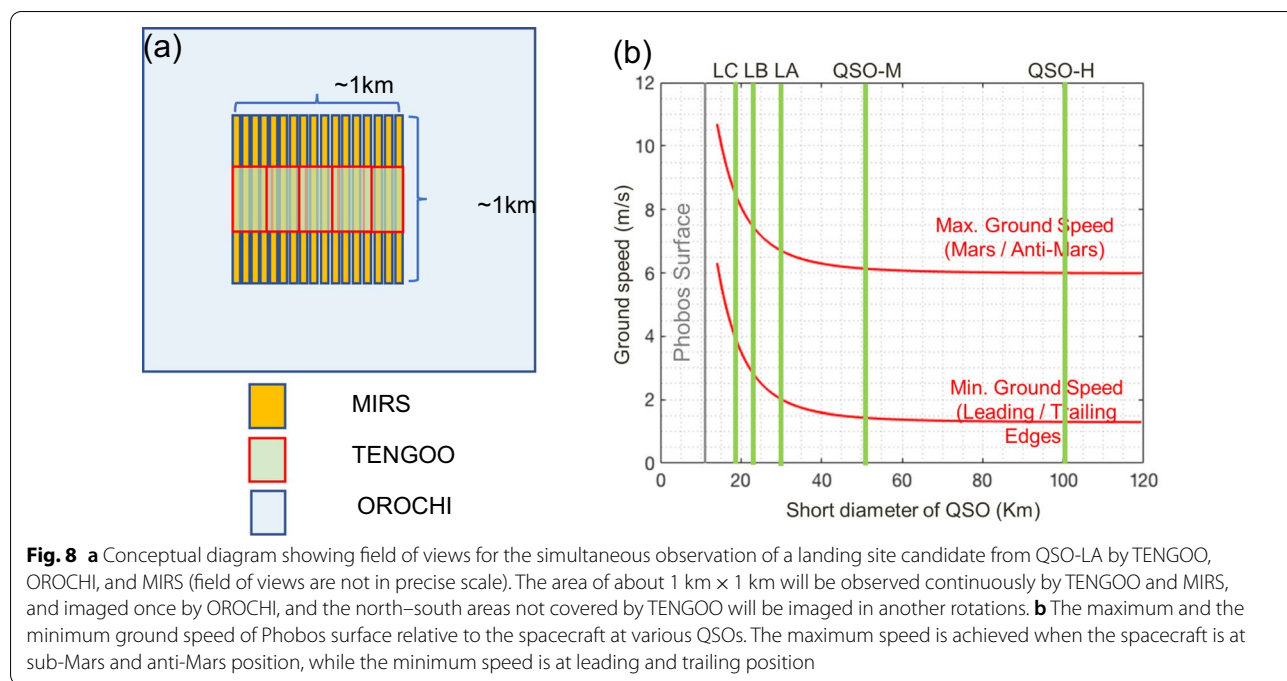observation except during Earth communication slots and during Phobos eclipses by Mars.

The best conditions for a spectral mapping by MIRS are met when the phase angle is around 10° and the local solar time around 12 h (low solar incident angles are preferred). To assess the best achievable performances, taking into account the spacecraft orbits, Phobos shape, time dependent system constraints, and MIRS field-of-view, we calculate for each facet of a detailed Phobos shape model the observation opportunity with the phase angle closest to 10°. To maintain a good geometric resolution, we limit the scan range of the mirror for the along-track amplitude of MIRS line of sight to $\pm 3°$ (compared to the $\pm 20°$ capacity).

QSO-H could be the opportunity to get a first global mapping of Phobos, with most of the areas within $\pm 30°$ of latitudes covered with 100 m resolution (Fig. 6a). Resolution is best for areas around 0° and 180° of longitude as the spacecraft closest approach to Phobos. Most of the South pole is not covered as it is very flat and consequently difficult to observe from an equatorial orbit. Figure 6b presents the percentage of Phobos surface covered (within $\pm 30°$ latitudes and all latitudes) as a function of the phase and sun incidence angles. We see that around 70% of Phobos surface could be covered with a phase angle close to 10°. Low sun incidence values have a positive impact on signal to noise ratios and we can see that 50% of Phobos' surface could be covered with a sun incidence angle of lower than 40° [this could be even lower (30°) for latitudes within $\pm 30°$].

QSO-M

For QSO-M we consider that five complete longitudinal coverages are necessary to obtain a global mapping by MIRS, one with each of the cross-track angles -6, $-3°$, 0°, 3°, and 6°. We add one longitudinal coverage to cover cross-track angles $-9°$ and 9° but only on half of the longitudes (around longitudes 0° and 180°) where Phobos polar angle is maximum. Figure 7b shows that around 90% of Phobos surface could be covered with a phase angle close to 10°. This value is better than that for QSO-H because of solar latitude is closer to 0 degree for QSO-M (Fig. 1 top). 50% of Phobos surface could be covered with a sun incidence lower than 45° [this could be even lower (20°) for latitudes within $\pm 30°$]. Sun incidence angle increases with the absolute value of the latitude, because the absolute value of solar latitude (β angle) is low at the time of this QSO-M (Fig. 1 top). Figure 7a shows that high resolution coverage could be satisfied with 38% of areas within $\pm 30°$ latitudes covered at geometric resolution of 20 m or better.

In addition to global mapping, the main objective of this first QSO-M in the period from November to December 2025 (Fig. 1 top) is to observe the 50 landing site candidates early enough to guarantee all their characteristics are transferred to the Earth before the solar conjunction during December 2025 and January 2026 (Fig. 1 bottom) so that a selection process can be applied to define the 20 best candidates that will be observed in greater details during QSO-LA in the period from February to March 2026 (Fig. 1 top). Data volume, data rate

Fig. 8 a Conceptual diagram showing field of views for the simultaneous observation of a landing site candidate from QSO-LA by TENGOO, OROCHI, and MIRS (field of views are not in precise scale). The area of about 1 km × 1 km will be observed continuously by TENGOO and MIRS, and imaged once by OROCHI, and the north–south areas not covered by TENGOO will be imaged in another rotations. **b** The maximum and the minimum ground speed of Phobos surface relative to the spacecraft at various QSOs. The maximum speed is achieved when the spacecraft is at sub-Mars and anti-Mars position, while the minimum speed is at leading and trailing position

Fig. 9 Coverage and geometric (spatial) resolution of MIRS mapping from QSO-LA (**a**), QSO-LB (**b**), and QSO-LC (**c**). Areas with resolution above 200 m are not displayed. **a** At QSO-LA, percentage of surface covered at resolution better than 100 m is 99% for areas within ±30° latitudes and 85% for all areas, at resolution better than 40 m is 99% for areas within ±30° latitudes and 75% for all areas, at resolution better than 30 m is 98% for areas within ±30° latitudes and 70% for all areas, at resolution better than 20 m is 92% for areas within ±30° latitudes and 58% for all areas, and at resolution better than 10 m is 37% for areas within ±30° latitudes and 21% for all areas. **b** At QSO-LB, percentage of surface covered at resolution better than 100 m is 92% for areas within ±30° latitudes and 67% for all areas, at resolution better than 40 m is 92% for areas within ±30° latitudes and 63% for all areas, at resolution better than 30 m is 91% for areas within ±30° latitudes and 61% for all areas, at resolution better than 20 m is 90% for areas within ±30° latitudes and 56% for all areas, and at resolution better than 10 m is 75% for areas within ±30° latitudes and 43% for all areas. **c** At QSO-LC, percentage of surface covered at resolution better than 100 m is 79% for areas within ±30° latitudes and 54% for all areas, at resolution better than 40 m is 79% for areas within ±30° latitudes and 52% for all areas, at resolution better than 30 m is 79% for areas within ±30° latitudes and 50% for all areas, at resolution better than 20 m is 79% for areas within ±30° latitudes and 48% for all areas, and at resolution better than 10 m is 71% for areas within ±30° latitudes and 41% for all areas

Nakamura *et al. Earth, Planets and Space*   (2021) 73:227

Page 11 of 27

Table 3 Observation conditions at four representative sites for phase angle closest to 10°

Site location (deg, deg)	QSO	Resolution[a] (m)	Phase angle (°)	Sun incidence (°)	Local solar time (h)
Lon 0°	LA	7	16	38	12
Lat 10°	LB	4	13	39	12
	LC	3	12	33	12.9
Lon 0°	LA	6	30	23	11.7
Lat −10°	LB	4	38	25	12.3
	LC	3	35	22	12.9
Lon 180°	LA	7	15	48	12
Lat 10°	LB	4	11	49	12.2
	LC	4	10	47	11.4
Lon 180°	LA	7	29	9	12
Lat −10°	LB	4	37	8	12.2
	LC	4	31	13	11.9

[a] Resolution by MIRS

transmission and duration of Earth communication slots will drive the capacity to perform the selection in due time.

QSO-Ls (QSO-LA, -LB, and LC)

The main objective on these QSOs is to characterize the landing site candidates as precisely as possible (Fig. 8a). The proximity to Phobos is an advantage for geometric resolution but it reduces the capacity to observe high latitude area. Also, the lower-altitude orbit has higher ground speed on Phobos (Fig. 8b) and in this case the MIRS along-track scanner will be used during observations to reduce the ground speed of MIRS line of sight projection on Phobos so that it is compatible with the integration time. Solar latitude (β angle) during QSO-LA, LB, and LC is negative (Fig. 1 top), because in this period summer comes to the southern hemisphere. Therefore, from QSO-LA, LB, and LC, the best observation with low solar incident and phase angle can be made for the southern hemisphere, while high latitude areas in the northern hemisphere are difficult to observe.

For the low altitude QSOs, we present in Fig. 9a–c for each facet of a Phobos shape model the observation opportunity with a phase angle closest to 10°. Again, along-track amplitude of MIRS line of sight is limited in that case to $\pm 3°$ to optimize geometric resolution. Spacecraft cross-track amplitude capacity is considered within $\pm 20°$ in the provided results. The percentage of Phobos surface covered from QSO-Ls (Fig. 9) is much fewer areas can be covered with an ideal phase angle compared to high and medium altitude QSOs (Figs. 6 and 7): 20% for QSO-LA and LB and 35% for QSO-LC of surface within ± 30 latitudes could be covered with a phase angle close

to 10°. For sun incidence, 50% of surface within $\pm 30°$ latitudes could be covered with an angle below 25° for QSO-LA and 30° for QSO-LB and LC.

On QSO-LA, landing sites candidates can be observed with excellent resolution (better than 20 m) as 92% coverage of $\pm 30°$ latitudes (Fig. 9a). On QSO-LB, resolution is improved to be better than 10 m as 75% coverage of area within $\pm 30°$ latitudes. However, for areas around 0° and 180° longitudes, MMX is too close to Phobos to reach $\pm 30°$ latitudes (Fig. 9b). On QSO-LC, percentage of $\pm 30°$ latitudes covered with 10 m or better resolution decreases with respect to QSO-LB due to the limitation of the visibility of high latitudes around 0° and 180° longitudes (Fig. 9c).

In Table 3, we present for four sites (towards and opposite to Mars and latitudes $\pm 10°$) the observation conditions for the opportunity with phase angle closest to 10°. We observe the phenomenon described above with higher sun incidence and lower phase angle on the north hemisphere and the opposite on the south hemisphere. To evaluate the variations of phase angle and surface temperature for precise determination of spectrographic and thermal inertia characterization, each site will be observed with several couples of phase angle and local solar times, in addition to the best combination of 10° phase angle and 12-h local time. To characterize the available couples, for 2 points located on longitude 0°, and at latitudes $\pm 10°$ we calculate all observation opportunities with a full along-track capacity of $\pm 20°$ provided by the MIRS scanner and a full cross-track capacity of $\pm 20°$ provided by the spacecraft. Figure 10 represents in the period of QSO-LB (Fig. 1 top) for each observation opportunity, the phase angle distribution as a function of the local solar time. We observe that: (1) phase angle is higher on south hemisphere; (2) for 12-h local time, maximum reachable phase angle is around 40° on north hemisphere, while it is 50° on south hemisphere, and (3) from 15-h local time, minimum reachable phase angle increases. For all the observation opportunities of these areas on QSO-LB, geometric resolution is between 4 and 7 m.

3D-QSO

Even in the QSO-H and QSO-M on equatorial plane (Figs. 6, 7, 8), some parts of the north pole and most parts of the south pole are not observable because of high viewing incidence angles or the masking by surrounding topology. This phenomenon is significant for QSO-Ls. On the other hand, 3D QSOs (Fig. 2b, c) allows a better coverage of the poles by reducing the viewing incidence angle at high latitudes. To achieve the visibility of all Phobos surface, an evolution within ± 30 km of vertical z component in Phobos fixed frame is required (Fig. 11).

Nakamura *et al. Earth, Planets and Space* (2021) 73:227

Page 12 of 27

Fig. 10 QSO-LB phase angle distribution as a function of local solar time for each observation opportunity for a landing site located at longitude 0° and latitude + 10° (in blue) or latitude − 10° (in red)
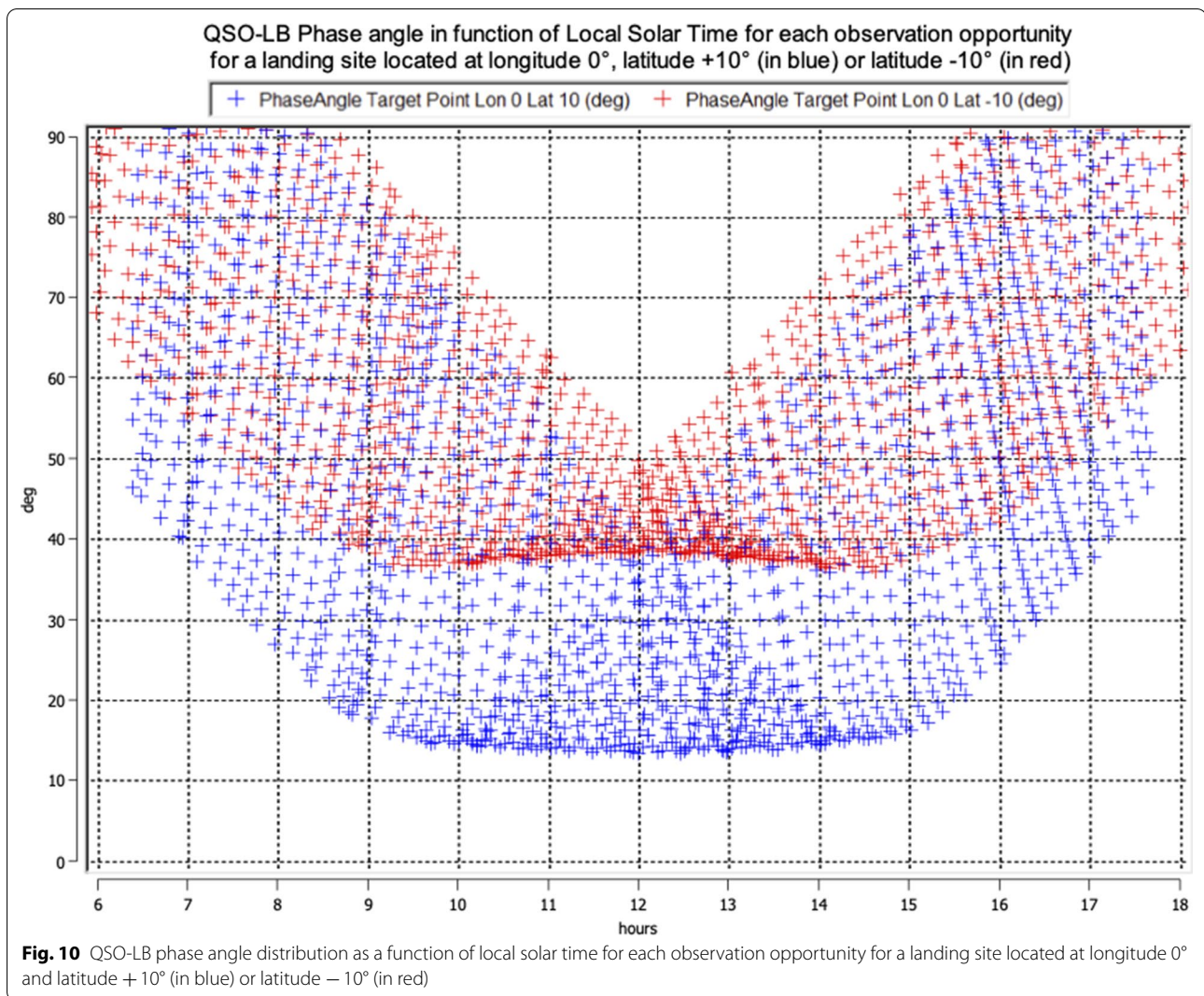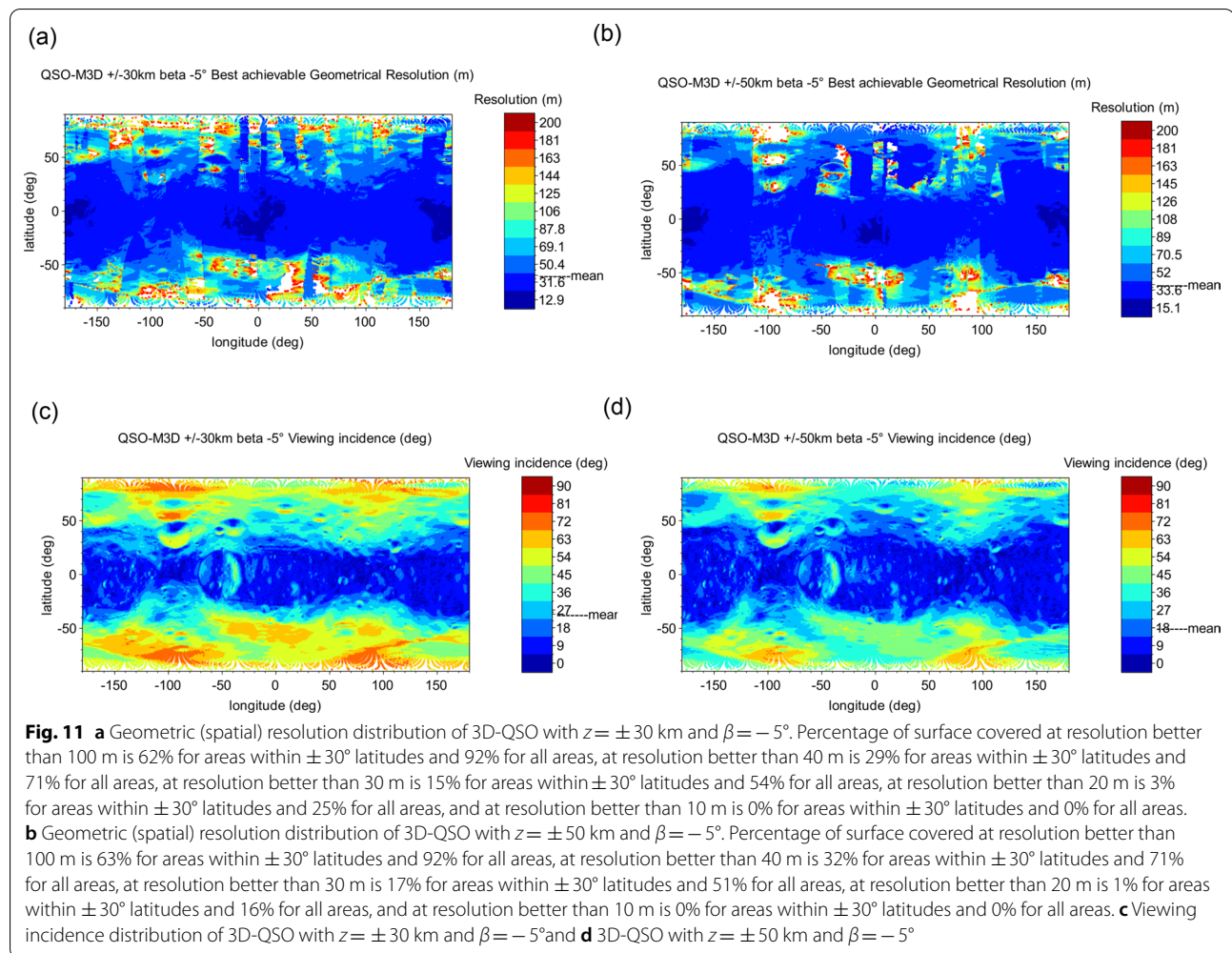
The higher the evolution of the z component in Phobos fixed frame, the lower the viewing incidence angle at poles can be achieved: 3D-QSO $z = \pm 50$ km is better for viewing incidence angle than $z = \pm 30$ km (Fig. 11c, d). The higher viewing angle can also reduce the geometric resolution of higher latitude areas of both northern and southern hemispheres (Fig. 11a, b).

The solar latitude for each QSO will depend on its time period or season (Fig. 1 top): again, to ensure a global observation of high latitude areas of both hemispheres, low absolute values of the β angles are recommended. This is illustrated on the Fig. 12a, b for the same 3D-QSO ($z = \pm 30$ km) with 2 values of β angles: $-5°$ and 21°, in which the latter shows lower sun incident angles for north pole areas. On the other hand, to observe one of the poles (not both poles) with high resolution, lower 3D-QSOs with lower z-values and high β angles would

significantly improve the geometric resolution of one of the polar regions: Fig. 12c, d shows comparison of geometric resolution with the same β angle ($+21°$) and different z values ($z = \pm 20$ km for Fig. 12c and ± 30 km for Fig. 12d), in which 3D-QSO with $z = \pm 20$ km is better in resolution of north pole areas. For 3D-QSO with $z = \pm 20$ km, 47% of the latitudes above 30° are covered with a resolution of 40 m or better, while for 3D QSO with $z = \pm 30$ km, 31% of the latitudes above 30° are covered with a resolution of 40 m or better.

As a consequence, one strategy (among others) with 3D QSOs is to have one high-z 3D QSO with a low absolute value of β angles to get a first overview of both poles and two low-z 3D QSOs with opposite high absolute value of β angles to get a detailed mapping of each pole. This strategy is also valid for TENGOO and ORO-CHI observations.

Nakamura *et al. Earth, Planets and Space* (2021) 73:227

Page 13 of 27

Fig. 11 **a** Geometric (spatial) resolution distribution of 3D-QSO with $z = \pm 30$ km and $\beta = -5°$. Percentage of surface covered at resolution better than 100 m is 62% for areas within $\pm 30°$ latitudes and 92% for all areas, at resolution better than 40 m is 29% for areas within $\pm 30°$ latitudes and 71% for all areas, at resolution better than 30 m is 15% for areas within $\pm 30°$ latitudes and 54% for all areas, at resolution better than 20 m is 3% for areas within $\pm 30°$ latitudes and 25% for all areas, and at resolution better than 10 m is 0% for areas within $\pm 30°$ latitudes and 0% for all areas. **b** Geometric (spatial) resolution distribution of 3D-QSO with $z = \pm 50$ km and $\beta = -5°$. Percentage of surface covered at resolution better than 100 m is 63% for areas within $\pm 30°$ latitudes and 92% for all areas, at resolution better than 40 m is 32% for areas within $\pm 30°$ latitudes and 71% for all areas, at resolution better than 30 m is 17% for areas within $\pm 30°$ latitudes and 51% for all areas, at resolution better than 20 m is 1% for areas within $\pm 30°$ latitudes and 16% for all areas, and at resolution better than 10 m is 0% for areas within $\pm 30°$ latitudes and 0% for all areas. **c** Viewing incidence distribution of 3D-QSO with $z = \pm 30$ km and $\beta = -5°$ and **d** 3D-QSO with $z = \pm 50$ km and $\beta = -5°$

OROCHI and TENGOO

QSO-H

Similar to MIRS, OROCHI observation aims to provide a global spectroscopic mapping by seven cameras with different band-pass filters with sufficient signal to noise level (>100, Kameda et al. 2021) to understand visible spectral variation and material distribution of Phobos. Because OROCHI has a wide field of view (Table 2), each image can cover from south to north polar regions from QSO-H and at the same time OROCHI observes Phobos with a sufficient spatial resolution similar to MIRS (Fig. 6a), because the two apparatuses have similar pixel size (Table 2).

OROCHI images will also contribute to spacecraft navigation and orbit determination, i.e., spacecraft attitude information can be obtained from the limb shape and/or the position of landmarks. If a wide-angle OROCHI image is simultaneously taken with a narrow-angle TENGOO image, it provides important context information

to the TENGOO image that helps shape modeling, i.e., which part of Phobos surface is imaged by TENGOO (Matsumoto et al. 2021).

The main objective of TENGOO observation at QSO-H is to construct a detailed shape model of Phobos at least within $\pm 30°$ latitudes. We limit latitudes to $\pm 30°$ because the spacecraft can land only on the areas close to the equator. Since TENGOO has very high spatial resolution (Table 2), the pixel resolution of TENGOO is better than 1 m even from 100 km distance, and thus it can resolve a few-meter scale targets on Phobos surface. Due to the high resolution, the TENGOO's FOV is narrower than 1°, while the apparent diameter of Phobos from QSO-H will be 5–10°. Therefore, latitudinal scan observations by TENGOO are planned to cover a region within $\pm 30°$ latitudes on Phobos. Such the latitudinal scan observation has advantages to limit observation local times and viewing angles on Phobos, which are essential for constructing a better shape model

Nakamura *et al. Earth, Planets and Space* (2021) 73:227

Page 14 of 27
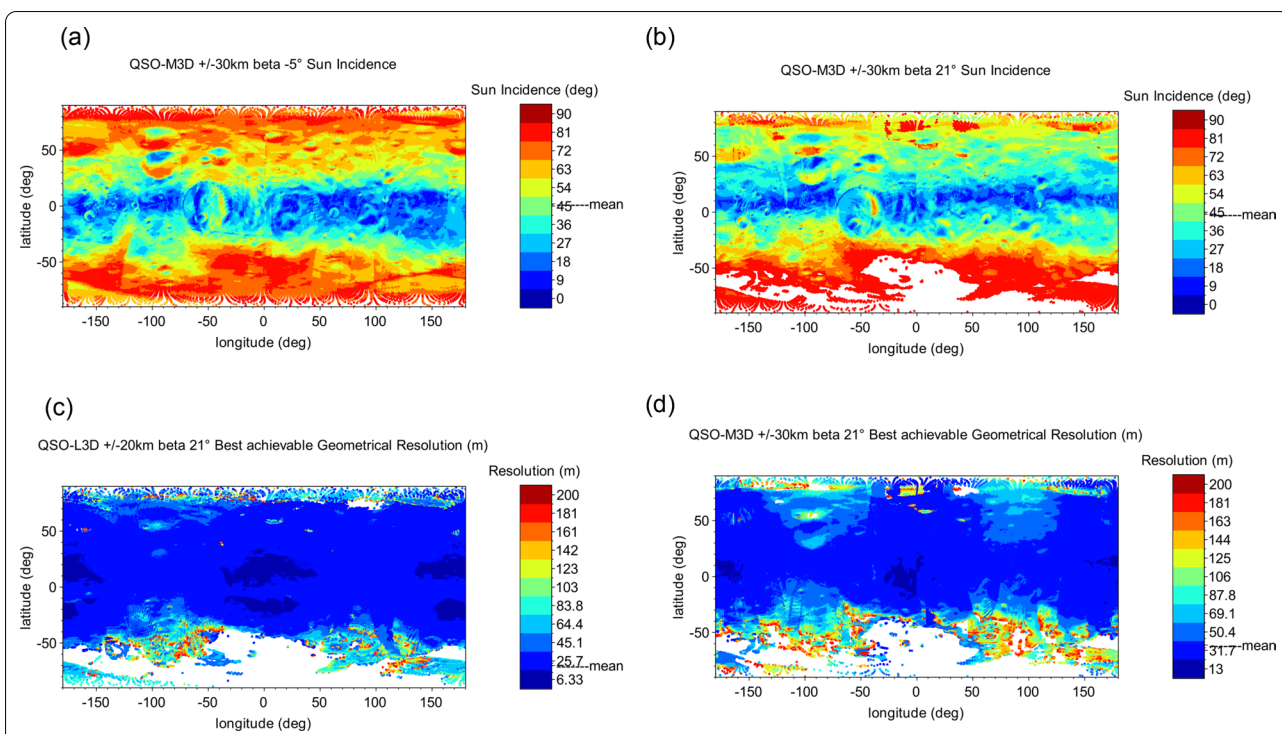
Fig. 12 Sun incidence angle distribution of **a** 3D-QSO with $z = \pm 30$ km and $\beta = -5°$ and **b** 3D-QSO with $z = \pm 30$ km and $\beta = 21°$. In **a** both poles can be observed with high Sun incidence angles, while in **b** Sun incidence is lower on North pole but most of south pole cannot be observed. **c** Geometric (spatial) resolution distribution of 3D-QSO with $z = \pm 20$ km and $\beta = 21°$. Percentage of surface covered at resolution better than 100 m is 58% for areas within $\pm 30°$ latitudes and 90% for all areas, at resolution better than 40 m is 47% for areas within $\pm 30°$ latitudes and 83% for all areas, at resolution better than 30 m is 43% for areas within $\pm 30°$ latitudes and 79% for all areas, at resolution better than 20 m is 32% for areas within $\pm 30°$ latitudes and 69% for all areas, and at resolution better than 10 m is 4% for areas within $\pm 30°$ latitudes and 23% for all areas. **d** Geometric (spatial) resolution distribution of 3D-QSO wit $z = \pm 30$ km and $\beta = 21°$. Percentage of surface covered at resolution better than 100 m is 52% for areas within $\pm 30°$ latitudes and 86% for all areas, at resolution better than 40 m is 31% for areas within $\pm 30°$ latitudes and 69% for all areas, at resolution better than 30 m is 21% for areas within $\pm 30°$ latitudes and 54% for all areas, at resolution better than 20 m is 6% for areas within $\pm 30°$ latitudes and 24% for all areas, and at resolution better than 10 m is 0% for areas within $\pm 30°$ latitudes and 0% for all areas. Areas in white cannot be observed because of spacecraft equatorial trajectory and Phobos flat shape on South pole. Areas with resolution above 200 m are not displayed

of Phobos. For the shape modeling, TENGOO plans to observe Phobos at least at three different local times; before, around, and after noon, such as 9.5 h, 12.5 h, and 14.5 h. For the local times of 9.5 h and 14.5 h, TENGOO will observe Phobos surface with three different viewing angles to satisfy a better stereo condition. Therefore, during the period in which MMX will stay on the dayside of Phobos in QSO-H (16 days in Table 1), TENGOO will observe whole longitudes of Phobos and the range of $\pm 30°$ latitudes with the seven different conditions (Matsumoto et al. 2021).

QSO-M

For QSO-M, OROCHI will observe all latitudes of Phobos simultaneously with the same geometric resolution as MIRS (Fig. 7) and acquire spectral data at the same local time and phase angles as MIRS with a better

spatial resolution than that from QSO-H. This makes it possible to connect OROCHI and MIRS spectra, and to obtain continuous visible and near-infrared spectra of each region of Phobos for more accurate identification of materials on the surface.

TENGOO will be used also for constructing the detailed shape model, though it will observe only regions where TENGOO observation will not be enough in QSO-H (Matsumoto et al. 2021). To reduce data volume and to match spatial resolutions of images observed in QSO-H and M, 2×2 pixels of a TENGOO image will be merged. In addition, TENGOO will monitor a detail surface condition on Phobos, such as finding small boulders and craters with a spatial scale of 1 m. Because such small objects can be recognized easily by their shadows and their heights can be measured from the shadows, TENGOO will observe the Phobos surface with Sun incidence angle equal to, or greater than, 60° for this purpose.

Nakamura *et al. Earth, Planets and Space*   (2021) 73:227

Page 15 of 27

Table 4 MEGANE required measurements from low-altitude QSO observations

Measurement	Global measurement of Phobos		Measurements of the "red" and "blue" units separately	
	Detection limit	Relative precision ($\pm 1\sigma$) (%)	Detection limit	Relative precision ($\pm 1\sigma$) (%)
H	100 ppm	20	100 ppm	33
O	20 wt%	33		
Mg	2 wt%	33		
Si	2 wt%	20	2 wt%	33
K	300 ppm	20	300 ppm	33
Ca	5 wt%	33		
Fe	1.5 wt%	20	1.5 wt%	33
Th	150 ppb	20		
A (average atomic mass)	n/a	33	n/a	33
Σa (thermal neutron absorption)	n/a	33	n/a	33

QSO-Ls

For TENGOO and OROCHI, the main observation objective on QSO-LA, LB, and LC is to characterize topographic and spectral features of the landing site candidates as precisely as possible for safe landing on a scientifically important site. From the viewpoint of the safe landing, TENGOO is the most important instrument because of its higher resolution to identify possible hazardous objects on the surface of Phobos. At 20 km altitude which is a typical altitude of QSO-LA, TENGOO resolution is 12 cm/px while OROCHI has 9 m/px. Therefore, TENGOO can resolve < 20 cm-scale boulders, craters, and regolith distribution from QSO-LA and 10 cm-scale targets from QSO-LC.

At QSO-LA, we plan to observe 20 landing site candidates. As shown in Fig. 8, one candidate area will be observed simultaneously by TENGOO, OROCHI, and MIRS whose field of view at 20 km altitude is 0.4 km × 0.3 km, 20 km × 23 km, and 1.15 km × 7 m, respectively. Target area to be observed is 1 × 1 km which can be covered with one OROCHI 7 color image, 3–4 TENGOO images (only in horizontal direction), and continuous observations by MIRS. We will conduct a longitudinal scan observation by TENGOO again to fill the vertical direction of 1 km × 1 km area (Fig. 12) when the observation point comes nadir on the next pass. For each candidate site, two or three longitude scans by TENGOO are planned.

To obtain reflectance spectra with signal–noise ratios (SNR) of higher than 100, OROCHI and MIRS needs exposure time of > 0.1 s. and > 2 s., respectively. At low altitude QSOs, Phobos' surface moves faster seen from the spacecraft (Fig. 8b). This requires that the distance during one exposure should be less than one pixel size of the instrument. At 20 km altitude, the ground speed of Phobos relative to the spacecraft is about 7 m/s (Fig. 8b),

while pixel sizes are 9 m and 7 m for OROCHI and MIRS, respectively, and thus exposure times are less than 1.3 and 1.0 s. for OROCHI and TENGOO, respectively. OROCHI can achieve SNR > 100, while for MIRS is difficult. As explained above, MIRS along-track scanner will be used during observations to reduce the ground speed of MIRS line of sight projection on Phobos to achieve exposure time > 2 s (= SNR > 100).

MEGANE
QSO-H

During QSO-H, MEGANE will acquire measurements for the purpose of characterizing the gamma-ray and neutron background. These MEGANE background measurements are planned to occur for a duration of 15 days, both before and after MEGANE's prime science measurements in the lower-altitude QSO-LB and QSO-LC. The MEGANE background measurements will occur simultaneously with other science observations. At QSO-M, no specific observation plan is scheduled.

QSO-Ls

During the lowest altitude QSO phase of the MMX mission, MEGANE will obtain gamma-ray and neutron measurements. These MEGANE measurements will determine the composition of Phobos and will contribute to determining Phobos' formation and to understanding the processes that have affected the moon's surface (Lawrence et al. 2019). The key measurements to be obtained by MEGANE during the low-altitude QSO phase of the MMX mission in 2026 are listed in Table 4. In addition to the required measurements and relative precisions given in Table 4, MEGANE may also provide measurements to determine the concentrations of additional elements, listed with their detection

Fig. 13 **a** Histograms of the altitude above Phobos' surface. **b** Plot of cumulative time at or below a given altitude, for QSO-LB and QSO-LC. Vertical lines mark altitudes of 1.0 and 1.5 Phobos radius values, which are related to MEGANE's measurement requirements. QSO-LB (**c**) and QSO-LC (**d**) altitudes as a function of Phobos latitude and longitude of the sub-spacecraft nadir point, colored by altitude. The general latitude range of the Phobos Blue Unit is marked with dotted lines. In all plots, the calculations take the irregular shape of Phobos into account, computing the radius of Phobos at the sub-spacecraft nadir point and ratioing it to the altitude to the surface at that same point

limits and relative precisions ($\pm 1\sigma$), if these elements are abundant enough on Phobos (Lawrence et al. 2019): Na (2 wt%, 30%), Cl (0.15 wt%, 25%), and U (50 ppb, 90%). Overall, MEGANE's observations will result in a bulk compositional measurement of Phobos as well as mapping of compositional variations on the surface of Phobos at a scale that will distinguish Phobos' "blue" unit from the more dominant "red" unit. As a general approximation, the spatial resolution of a gamma-ray or neutron investigation is proportional to the altitude, i.e., an altitude of 10 km yields a full-width at half-maximum spatial resolution of ~10 km. In QSO-LC, the altitude above Phobos' surface ranges from roughly 6.7 km to 16 km. Specific details and examples of MEGANE's expected spatial mapping that take into account the irregular shape of Phobos are shown in Chabot et al. (2021).

Driving operational requirements for MEGANE to obtain the sensitivity required for the measurements listed on Table 4 are the altitude at the time of MEGANE's observations and the total accumulated measurement time. Analysis of previously flown gamma-ray instruments and their resulting science measurements has shown that cumulative measurement times of ≥ 10 days at altitudes ≤ 1 body radius are required to ensure measurements with sufficient sensitivity to meet MEGANE's

Nakamura *et al. Earth, Planets and Space*   (2021) 73:227

Page 17 of 27

science measurement objectives (Peplowski 2016). The neutron spectrometer measurements of MEGANE have less strict altitude requirements than the gamma-ray spectrometer measurements, requiring altitudes ≤ 1.5 body radius to meet MEGANE's neutron spectrometer measurement objectives. Both gamma-ray and neutron spectrometer measurements are used in combination to produce the compositional results listed in Table 4. MEGANE's operational plan requires a 50% margin in the total accumulated measurement time that is planned, bringing this overall driving operational requirement to be a plan that includes ≥ 15 days of total accumulated MEGANE measurements at ≤ 1 body radius.

Both QSO-LB and QSO-LC offer opportunities for MEGANE to acquire data at altitudes ≤ 1 body radius, as shown in Fig. 13. In particular, QSO-LB enables observations at ≤ 1 body radius for 32% of its QSO, with a minimum altitude of about 0.6 body radius, and QSO-LC is at ≤ 1 body radius for 47% of its QSO, with a minimum altitude of about 0.5 body radius. Thus, QSO-LC is much better suited for MEGANE to meet its science measurement objectives. If the MMX spacecraft only pointed nadir at Phobos all of the time, an unrealistic scenario, it would take roughly 47 calendar days to achieve the required MEGANE total cumulative measurement time of 15 days at ≤ 1 body radius from QSO-LB. This time is reduced to 32 days to achieve a total cumulative measurements time of 15 days at ≤ 1 body radius from the lower altitude QSO-LC.

However, the MMX spacecraft will not always be pointed nadir during the time planned to be spent at the combined QSO-LB and QSO-LC phase. In particular, the need to keep direct sunlight off the instrument deck may lead to Phobos-pointed observations only occurring on the Phobos dayside, which decreases the possible measurement time for MEGANE by a factor of two. The spacecraft will also need to point away from Phobos nadir for uplink and downlink with Earth. If these Earth communications can be conducted when the spacecraft is over the Phobos nightside, that would not be an additional loss of nadir-pointing time for MEGANEd. MEGANE is mounted on the instrument deck of the spacesraft and designed to obtain the required sensitivity of its science measurements when pointed within 10° of nadir. If the operations of other instruments require off-pointing beyond 10° of nadir, this would further reduce MEGANE's accumulated measurement time.

Given the lower altitude of QSO-LC in comparison to QSO-LB, QSO-LC is best suited to achieve MEGANE's measurement objectives and provides more robust margin against other off-pointing operations.

Phobos' irregular shape and the nature of QSO-LB and QSO-LC result in uneven coverage of all Phobos longitudes at low altitude, as shown in Fig. 13c, d. In QSO-LB and QSO-LC, the majority of MEGANE's coverage is limited to latitudes of roughly ± 20° of the equator (Chabot et al. 2021), and Phobos' polar regions will not be measured by MEGANE. For both low-altitude QSO options, the "blue unit" is measured by MEGANE at altitudes ≤ 1 body radius, which will enable the determination of compositional differences between the "red" and "blue" unit as detailed on Table 4. However, in QSO-LC, all longitudes are measured by MEGANE at altitudes ≤ 1.5 body radius, enabling neutron spectrometer compositional measurements across all Phobos longitudes, such as H content, average atomic mass, and thermal neutron absorption. This is a further advantage of obtaining MEGANE measurements from the lower altitude QSO-LC option. Phobos' irregular shape (Ernst et al. 2021) will also factor into the analysis of the MEGANE measurements, such as the footprint on the surface and the resulting mapping abilities, as discussed in Chabot et al. (2021).

While MEGANE's most important science requirements given in Table 4 will be achieved during this low-altitude QSO phase in 2026, future phases of the MMX mission that achieve low altitudes may provide compelling opportunities for additional MEGANE science measurements. Such opportunities could include measurements during rehearsal or actual descents and/or ascents to the Phobos surface, during rover delivery activities, and while the spacecraft is on the surface of Phobos. These science opportunities beyond the low-altitude QSO phase could link the scale of MEGANE's global QSO compositional measurements and the samples to be brought back to Earth by the MMX mission.

MSA
QSO-H
The Mass Spectrum Analyzer (MSA) consists of an ion energy mass spectrometer and two magnetometers, which measure velocity distribution functions and mass/charge distributions of low-energy ions and the magnetic field of the solar wind, respectively (Yokota et al. 2021). The MSA will perform in-situ observations of all the ions going towards and coming from Phobos to investigate the Phobos surface and related phenomena (e.g., space weathering). Figure 14 schematically shows the MSA observation in the Phobos-centric Solar Ecliptic coordinates. The solar wind is the dominant source of ions incident on the Phobos surface, while escaping ions from the Martian atmosphere reach there when Phobos is in the tail or plume region of Mars. As for the ions from Phobos, MSA will measure solar wind ions scattered at the surface and secondary ions from the surface sputtered by the solar wind. It is expected that secondary ions

Nakamura *et al. Earth, Planets and Space* (2021) 73:227

Page 18 of 27
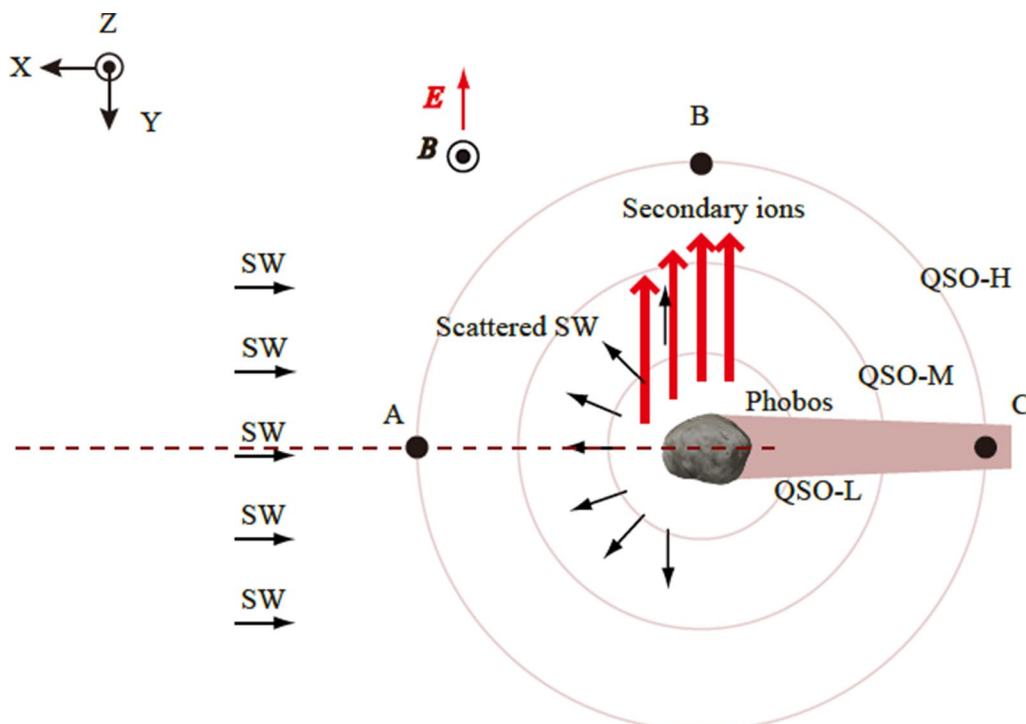
Fig. 14 Observation configuration of MSA in the Phobos-centric Solar Ecliptic coordinates. The Phobos-centric Solar Ecliptic coordinate system has the *X*-axis pointing from Phobos towards the sun, the *Z*-axis parallel to the ecliptic northern pole, and the *Y*-axis determined in the right-handed system. In both panels, *B* and *E* indicate the magnetic and electric fields of the SW, respectively. The magnetometer measures *B*, while *E* is derived from $E = -V \times B$, where *V* denotes the SW velocity nearly towards the $-X$ direction

sputtered by the solar wind, especially Mg^+, Si^+, Ca^+, and Fe^+, maintain the surface chemical composition (Elphic et al. 1991; Schaible et al. 2017). In addition, the MSA has opportunities to observe water-related ions generated from the Martian torus if exits.

In the dayside of Phobos in the QSOs from the subsolar point (point A) to the terminator (point B), the MSA that has a hemispherical field-of-view can measure both solar wind ions and those scattered at the surface. It should be noted that the observation of the solar wind ions is occasionally interrupted by the spacecraft's structure depending on its attitude. Even in the QSO-H, scattered solar wind ions can reach the spacecraft, because they retain around 50% of the incident energies when being scattered (Saito et al. 2008). The scattered ions are picked up by the solar wind again and travel downstream of Phobos. Moreover, some of them intrude the void region (point C) that is shielded from the solar wind (Nishino et al. 2010).

Since the initial energy of secondary ions sputtered from Phobos is negligible, they almost move along the solar wind electric field (*E*) to the spacecraft altitude (Yokota and Saito 2005). Thus, the opportunity to observe

secondary ions from Phobos is limited near the terminator (point B), while the direction of *E* is another requirement. The information of *E* is given by $E = -V \times B$, where *V* and *B* indicate the solar wind velocity and magnetic field, respectively. Both of them are measured by the MSA ion analyzer and magnetometers. Since *V* is approximately in the $-X$ axis, *E* is restricted to the *YZ* plane. When the spacecraft is around the terminator, the possibility of *E* directing from Phobos to the spacecraft is below ~5% in the QSO-H. Assuming the direction of *B* is non-biased, the possibility is approximately given by $d/2\pi L$, where *d* and *L* denote the diameter of Phobos and spacecraft's altitude, respectively. The sputtering points of the measured secondary ions can be traced back using estimated *E*, though the spatial resolution is comparable to the spacecraft's altitude.

QSO-M
The MSA observation in the QSO-M is the same as that in the QSO-H, especially for solar wind ions. However, the opportunity of observing scattered solar wind ions and secondary ions from Phobos will increase as the distance between the spacecraft and Phobos decreases.

Nakamura *et al. Earth, Planets and Space*   (2021) 73:227

Page 19 of 27

Observations of scattered solar wind ions provide more information about the ions immediately after their scattering. The observation in the QSO-M increases the possibility of E directing from Phobos to the spacecraft in the terminator to ~10%. The scattering and sputtering points of the measured ions will be more accurately determined as the altitude decreases.

QSO-Ls

In the QSO-LA, LB, and LC, the MSA will derive much more information on the Phobos surface from the observation of scattered solar wind ions and secondary ions from Phobos. The possibility of adequate E to observe secondary ions from Phobos in the QSO-Ls goes up to 10 s % for the spacecraft around the terminator. Thus, the QSO-Ls will ensure the observation period especially for secondary ions from Phobos. Moreover, the MSA observation in the QSO-Ls will provide the distribution maps which divide the Phobos surface to several areas because the spatial resolution of scattering and sputtering points reduces to around the spacecraft's altitude. If there are electromagnetic effects similar to those of the Earth's Moon, such as magnetic anomalies (e.g., Tsunakawa et al. 2015) or surface charging (e.g., Stubbs et al. 2014), low-altitude observation of ions and magnetic field with the MSA will reveal their associated phenomena (Saito et al. 2012). The situation of the MSA observation in the 3D-QSO is the same as that in the QSO-M because the ion observation is mostly determined by the spacecraft' altitude and solar wind conditions. However, similar to other remote-sensing instruments, the MSA will obtain an opportunity to observe ions scattered or sputtered in the polar region of Phobos.

CMDM

The CMDM consists of a sensor with a sensitive area of $1~m^2$ and an electronics box, which measures the collisional momentum with which a dust particle impacts the sensor of the CMDM (Kobayashi et al. 2018) and its only observation mode is to wait for the signal from the dust particles in orbit to collide with the sensor. The main objective of the CMDM is to detect undiscovered Mars-orbiting dust ring particles in place. According to theoretical predictions from previous studies (e.g., Ishimoto 1996; Hamilton 1996; Krivov and Hamilton 1997), Martian dust rings would be formed as a result of the injection into Martian orbit of particles with initial velocities exceeding escape velocities out of ejecta released by meteoroid bombardment of the surface material of Phobos (or Deimos). The freshly ejected dust particles orbit Mars in a nearly Phobos or Deimos orbit. However, the ring particles are perturbed mainly by solar radiation, and their orbits evolve and their eccentricity gradually

changes. In the case of dust particles smaller than 20 μm, their eccentricities change so much that they collide with the Martian atmosphere and would be lost from the orbit within a short time (Ishimoto 1996; Hamilton 1996; Krivov and Hamilton 1997; Liu and Schmidt 2020). At the position of Phobos orbit, we will be able to observe not only dust particles of Phobos origin, but also dust particles of Deimos origin whose orbits have evolved to have their pericenters at or inside Phobos orbit.

QSO-H and QSO-M

When the orbit of the spacecraft is at QSO (almost the same orbit as Phobos in the Mars fixed coordinate system), ring particles with orbits evolved from the Phobos orbit will impact the spacecraft in the ram or wake direction with velocities of less than 1 km/s (Krivov and Hamilton 1997). The CMDM sensor is mounted on the $-X$ panel of the spacecraft. Therefore, we expect the CMDM to detect more ring particles when its sensor is pointing in the direction of the ring particles' arrival (the ram or wake direction of the spacecraft). On the other hand, when the CMDM sensor points to the apex of Mars, it will detect interplanetary dust in Keplerian motion around the Sun. The interplanetary dust and ring particles that exist as this background are distinguished by the arrival direction.

According to theoretical studies (e.g., Ishimoto 1996; Hamilton 1996; Krivov and Hamilton 1997), the phase of the peri- and apocenter in the orbit of ring particles around Mars depends on the size of the ring particles and varies with the seasons. Therefore, when performing in situ observations on QSOs, CMDMs may observe changes in the flux of dust particles depending on their orbital position. Since the spatial distribution of Martian ring dust is very rare, to reveal its existence and distribution, the CMDM should be turned on as constantly as possible in any orbit to wait for dust particles to impact the sensor. Since the ring structure is much larger than the difference between QSO-H and QSO-M, no difference in the collision frequency of dust particles will be observed in either orbit.

QSO-Ls

Compared to QSO-H and QSO-M, the distance to the spacecraft from the surface of Phobos is lowered to about 10 km in QSO-L (Table 1). As mentioned above, there is continuous meteoroid bombardment on the surface of Phobos, and this bombardment should result in the existence of ejecta clouds. Such ejecta dust clouds have been observed in the vicinity of Ganymede (Krueger et al. 1999) and the Moon (Horanyi et al. 2015). Among such dust particles, those that exceed the escape velocity of Phobos (about 11 m/s) are

Nakamura *et al. Earth, Planets and Space*   (2021) 73:227

Page 20 of 27

Fig. 15 Baseline delivery strategy of Rover which is released at 40 m high from the surface of Phobos. Red trajectory indicates spacecraft and blue is rover
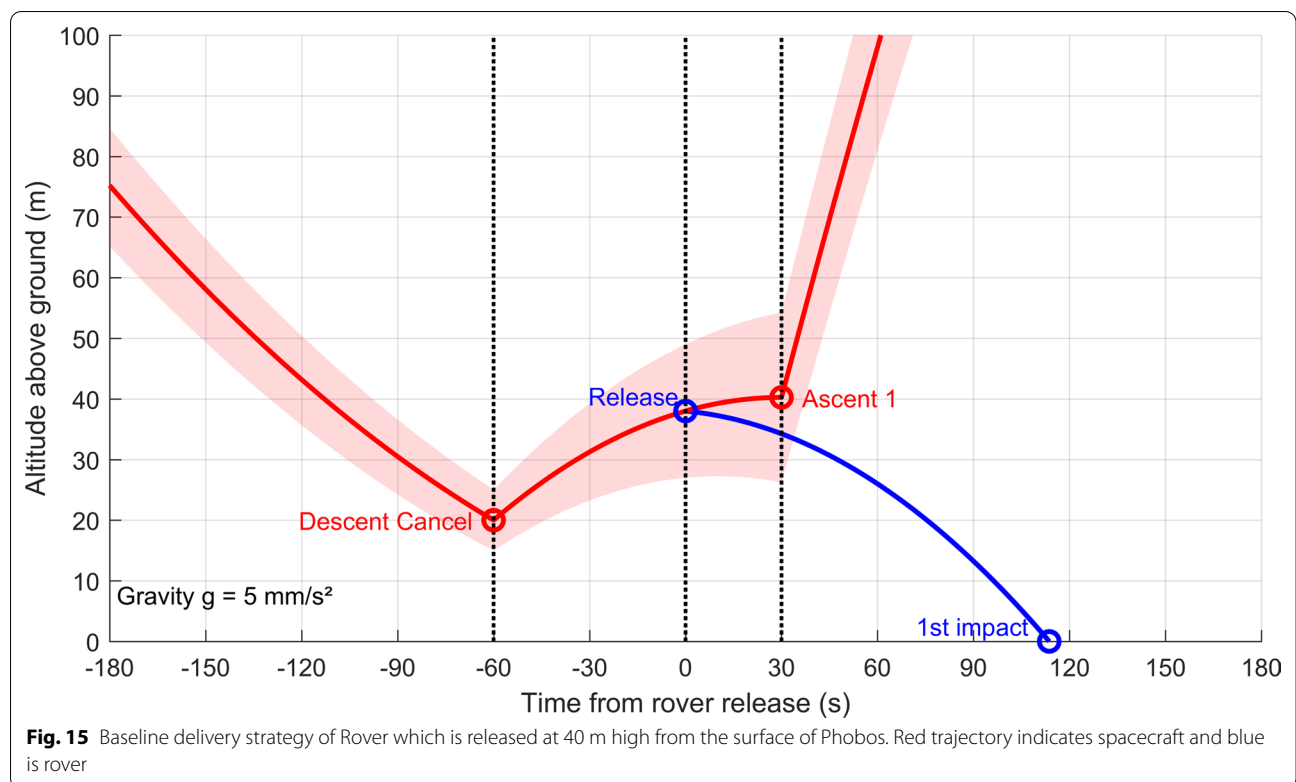
injected into the Martian orbit and become part of the rings, while those that do not exceed the escape velocity return to the Phobos surface. The collisions of the Phobos (or Deimos) surface with ring particles, once ejected from the Phobos gravitational field, may be the most significant source of dust contribution (Sasaki 1999). Because of the existence of these dust particles, CMDM may observe higher fluxes during QSO-Ls than QSO-H and QSO-M.

3D-QSO

In-situ observation of CMDM on 3D-QSO may reveal the distribution of dust particles in the thickness direction of the Phobos dust ring. The ring of Phobos is very thin, and the amplitude of the tilt variation is as small as 1° (Ishimoto 1996) that corresponds to about 170 km (or even smaller) at Phobos' orbit. In 3D-QSO, the orbit of the MMX spacecraft has an inclination angle from the equatorial plane, so it may be possible to see the latitudinal variation of the dust number density. This observation data can be used to discuss the thickness of the Phobos dust ring.

LIDAR

The spatial resolution of LIDAR observation is decided by the laser footprint size on the Phobos'

surface. Because the beam divergence of LIDAR laser is 0.5 mrad (Table 2), the laser footprint size becomes 50 m when the altitude of spacecraft is 100 km (QSO-H), and less than 10 m when the altitude of spacecraft is below 20 km (QSO-L). From QSO-H, LIDAR observes the surface topography with spatial resolution of 50 m, which provide the global morphology such as cross-sectional view of Stickney and other large craters on Phobos. Because LIDAR observations are sensitive to the altitude change, E–W asymmetricity of craters would be detected if present (see Hirata et al 2021).

From QSO-M, the footprint size of LIDAR becomes 25 m. With this spatial resolution the grooves on Phobos (80–200 m width; Rosenblatt 2011; Basilevsky et al. 2014) can be resolved. The cross-sectional view of the grooves will give us important information related to their origin and evolution. From QSO-L, LIDAR observes the morphology of Phobos with a spatial resolution of less than 10 m and thus can provide critical information on the landing site selection (Senshu et al. 2021). The height of boulders in and around the landing site candidates will be obtained by the LIDAR observations. At the same time, the compositional heterogeneity could be observed from the reflectance

Nakamura *et al. Earth, Planets and Space* (2021) 73:227

Page 21 of 27

Fig. 16 Rover delivery to the Phobos surface and up-right strategy
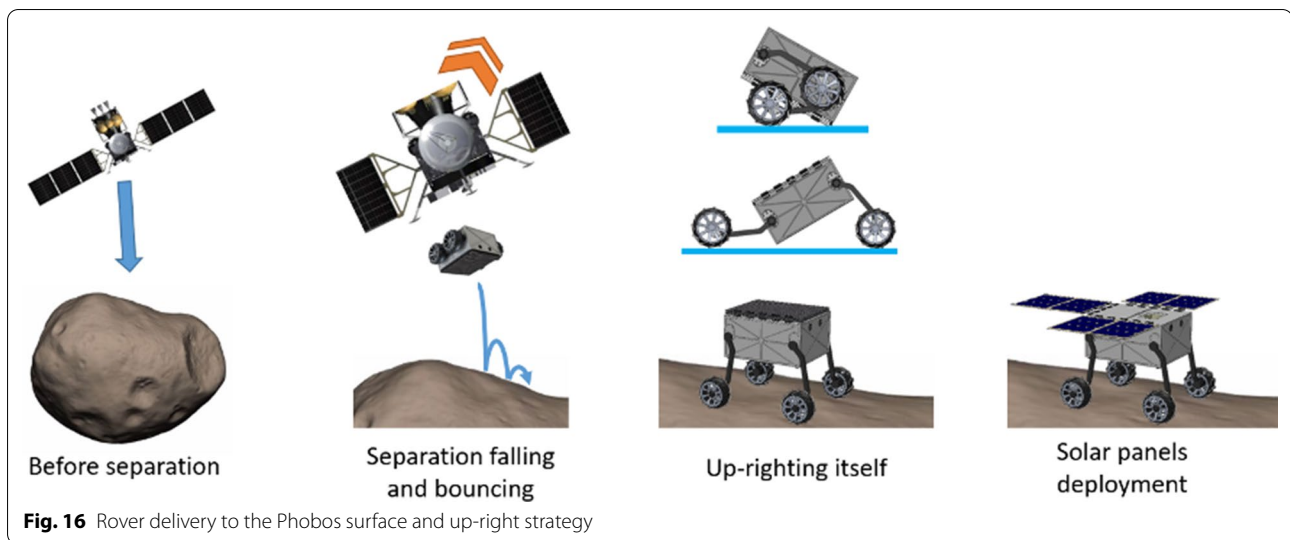
Table 5 Instruments on MMX rover

Instrument	Type	Measurement	Responsible institution
NavCAM	Stereo navigation cameras	Local environment Multi-scale imaging Path selection for driving	CNES (with LAM)
WheelCAM	Two cameras imaging interaction of wheels with soil	Soil characteristics, strength, cohesion, grain size (> 200 µm)	CNES (with ISAE-SUPAERO)
RAX (Cho et al. 2021)	Raman spectrometer	Mineralogical composition, grain heterogeneity	DLR (with INTA/Univ. Valadolid, JAXA/Univ. Tokyo)
MiniRAD	Radiometer	Thermal properties (temperatures, conductivity, capacity), porosity	DLR

measurement by LIDAR. The reflectance is geometric albedo at 1 µm wavelength because of phase angle of the measurement is 0°.

Rover and its deployment on Phobos

The MMX Rover, a mobile surface science package, provided by CNES and DLR with contributions from Spain and Japan (Michel et al. 2021; Ulamec et al. 2019) is planned to be delivered to the surface of Phobos during a landing rehearsal of the main spacecraft. The rover will determine the physical and mineralogical properties of the undisturbed Phobos surface material and the heterogeneity within the landing and roving area. Moreover, it will also observe the flow of the surface regolith on the wheels, and therefore will give precious information on the dynamics of the regolith in the actual gravitational environment of the surface. The whole set of Rover measurements will thus also support the main scientific objectives of MMX mission by providing data that can be used for preparing the landing sites of the main spacecraft as well as the sampling procedure.

The Rover will be released at an altitude of less than 100 m (the current baseline scenario assumes 40 m: Fig. 15) and free-fall without attitude control to the surface. After impact onto the Phobos surface at a speed less than 1 m/s, the rover is expected to bounce several times until coming to a complete rest (Fig. 16). The exact sequence of the deployment of the locomotion system (i.e., unfolding of "legs" with wheels) will upright the rover, independent of its original attitude. The scenario does have some similarity with MASCOT, the small lander delivered to asteroid Ryugu as part of the Hayabusa2 mission, which was also autonomously uprighting itself after a short bouncing phase (Jaumann et al. 2019; Ho et al. 2021). After the Rover is positioned on its four wheels, the solar generator is going to be deployed, and the vehicle can start science operations after a short commissioning phase (Fig. 16). Operations on the surface of Phobos are planned for > 100 (Earth) days, and the timeline will be optimized, sharing periods of mobility ("driving") and science measurements with the four PI-led instruments (see Table 5 and Michel et al. 2021 for details).

Nakamura *et al. Earth, Planets and Space*   (2021) 73:227

Page 22 of 27
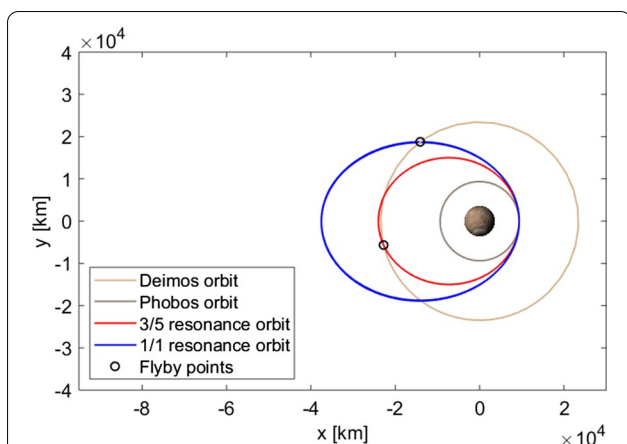
Fig. 17 Flyby orbits for Deimos observations with Mars centered. Example sequence: from an orbit with 3/5 resonance to an orbit with 1/1 resonance, before finally escape from Martian system. With respect to a fixed Mars, the Sun appears to rotate in the counter-clockwise direction and the spacecraft revolves in clockwise direction
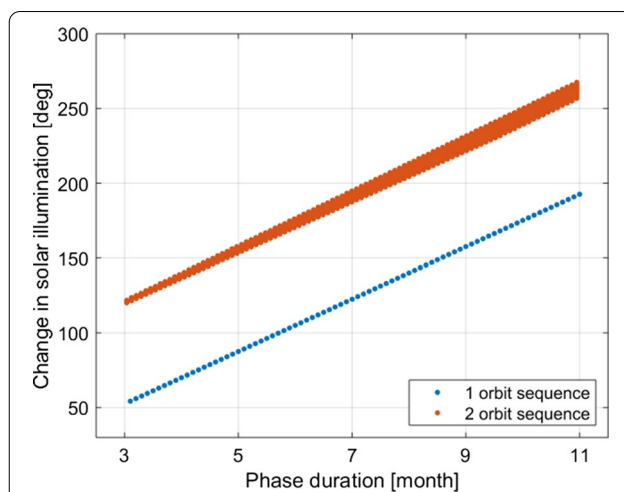
Fig. 18 Approximate achievable change in solar illumination for the case of a single 3:5 resonant orbit (1 orbit sequence) or a combination of 3:5 and 1:1 resonant orbits (2 orbits sequence) as a function of time duration in month. The latter offers different amount of total change depending on how many are flybys performed at each of the two orbits

Note that for thermal and power reasons, the rover is sensitive to eclipses by Mars. Thus, a landing site on the far side from Mars is envisaged. The landing site selection for the rover will take place in close alignment with the sampling site selection procedure, as similar products are required for both (high resolution images, detailed shape model, LIDAR data on surface roughness) and the rover delivery is planned to be performed at the location where the rehearsal for the first MMX touch down (possibly for TD1) is going to take place.

Basic strategy of scientific observation plan for Deimos from flyby orbits

Deimos observation can occur before insertion to Phobos orbit and after leaving it, which corresponds to phase 1 and phase 5, respectively (Fig. 1). However, the current schedule cannot allow the spacecraft to use a long time for Deimos observations before insertion to Mars orbit. Therefore, the main Deimos observations are planned to be performed in phase 5 for approximately 4 months. To minimize fuel consumption during this phase observations of Deimos will occur via multiple flybys. No rendezvous or landing operations on Deimos are planned. For multiple flybys, the spacecraft will be placed on a resonant orbit that reencounters Deimos periodically (Fig. 17). Throughout the trajectory to escape from Mars, the spacecraft will travel on a number of orbits around Mars and crossing Deimos' orbit periodically. The selected resonance determines the size of the orbit and the relative velocity between the spacecraft and Deimos during each flyby. A lower relative velocity translates into

a lower ground speed resulting in higher spatial sampling of Deimos surface.

Deimos is tidally locked, meaning that it always presents the same face toward Mars. This is an aspect to consider in the design of flyby orbits, because it constrains the observable regions of Deimos. That is, the longitude of the closest approach upon a single flyby is determined by the relative velocity between the two bodies, which is determined by the chosen resonance. Additionally, the synchronous motion between Mars and Deimos also constrains the regions of the moon that are illuminated by the Sun, which affects the observation strategy for some of the instruments onboard.

Depending on the duration of the Deimos observations, the change in the Sun's position with respect to Deimos' surface might be insufficient to observe different regions on the moon. This issue can be addressed using multiple resonant orbits. Since each resonant orbit intersects with Deimos twice (namely, there is an outgoing flyby and an incoming flyby), a combination of resonant orbits can be used where opposite flyby intersection points are used, as depicted in Fig. 17. This does not incur additional delta-V as long as subsequent orbits are used in ascending order of size because the spacecraft will escape from Mars in any case. The difference in true anomaly between the intersection points, which varies contrary to the apparent counter-clockwise rotation of the Sun, contributes to the change in the illuminated region of the moon. Different orbits also provide different longitudes on Deimos surface at the point of closest approach. As seen in Fig. 17,

Fig. 19 Spacecraft's ground track of the first flyby on a 3:5 resonance orbit (**a**), the last flyby on a 3:5 resonance orbit (**b**), and the last flyby if a change to a second 1:1 resonance is performed (**c**)
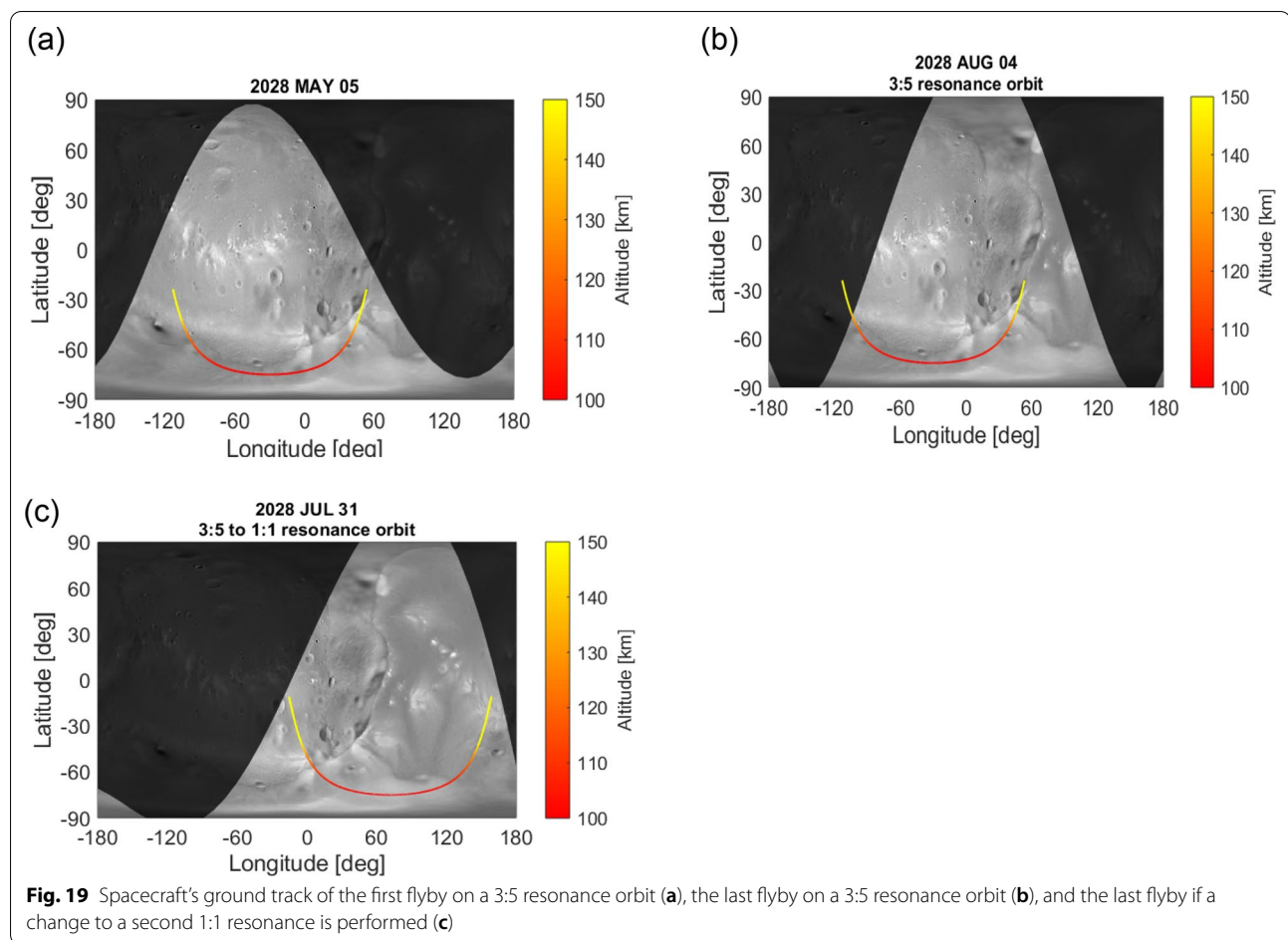
larger changes in true anomaly between flyby points yield larger changes in solar illumination angle but also means larger orbits. The latter is not desirable because it implies higher relative velocities during flybys; the scientific observation of Deimos benefits from low velocities during each passage instead.

For a duration of 4 months in phase 5 (Fig. 1 top), the change in solar illumination is approximately 70°. This change is effectively reflected as the change in longitude of the Sun's direction on Deimos surface between the first and last flyby. If we increase the period of Deimos observation to include 7 months of Phase 4 (Fig. 1 top), then the phase durations becomes 11 months and a single 3:5 resonance orbit provides an approximate change in the solar illumination of about 190°. If such an orbit is combined with a larger 1:1 resonance orbit, the same change can be obtained in a time period of less than 7 months. Additional combinations can be seen in Fig. 18.

These changes in solar illumination are shown in Fig. 19a–c. They show the spacecraft's ground track on the surface of Deimos for the first flyby in a 3:5 resonance orbit, the last flyby in the same orbit, and an alternative last flyby if a switch to a 1:1 resonance orbit is performed, respectively. Figure 19b, c reflect the additional change in sun's direction obtained by making use of multiple resonant orbits instead of using a single orbit throughout the sequence.

TENGOO, OROCHI, and MIRS

TENGOO, OROCHI, and MIRS will observe Deimos from flyby orbit during the passage close to Deimos. If we take a 3:5 resonance orbit (Fig. 17), the spacecraft encounters Deimos with a 90-h interval, equivalent to three rotations of Deimos around Mars. The relative velocity to Deimos surface at the closest approach is 0.377 km/s. If we use a 1:1 resonance orbit (Fig. 17), the spacecraft encounters Deimos with a 30-h interval with the relative velocity of 0.855 km/s. The closest distance to Deimos is adjustable: first approach could be 1000 km away from Deimos, but with increasing times of flybys which improve the precision of orbits of both Deimos and the spacecraft, the spacecraft is able to come closer to Deimos finally with 100 km distance.

Nakamura *et al. Earth, Planets and Space* (2021) 73:227

Page 24 of 27

Fig. 20 MIRS geometric resolution (m) in function of time (s) for the 2 resonant flyby trajectories with a 300 km closest approach. Red line shows 3:5 and blue shows 1:1 resonance orbit. The spacecraft is closest to Deimos at $t=0$
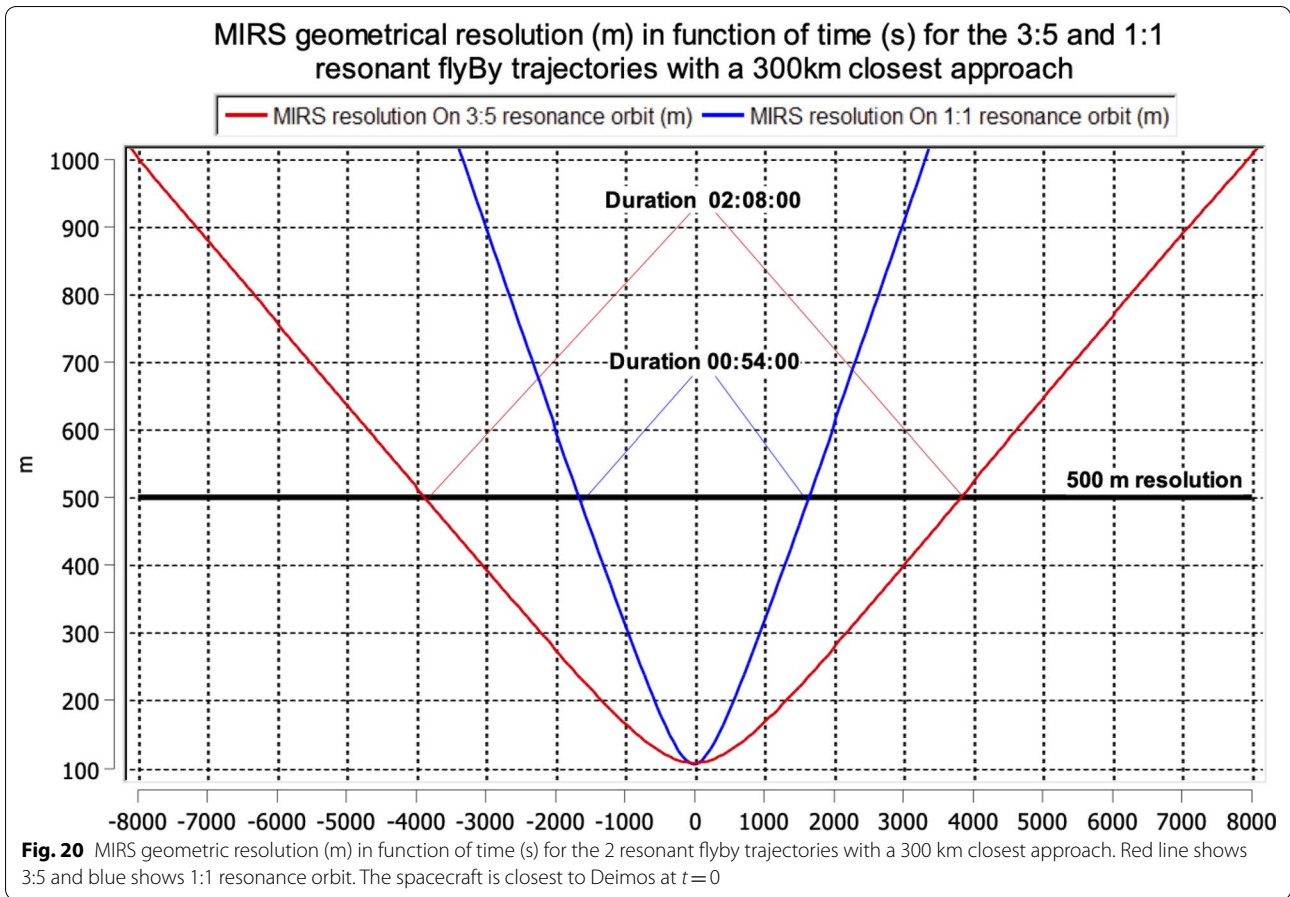
FOVs at 100 km distance are 100 km × 115 km for OROCHI, 5.75 km × 35 m for MIRS, and 2.0 km × 1.5 km for TENGOO. Therefore, only OROCHI can cover all of Deimos illuminated area with single flyby, but multiple flybys are required for MIRS and TENGOO. It is possible to change the position of closest approach to the northern or southern direction at every flyby and thus the areas with wider latitude range can be covered with observation by both MIRS and TENGOO.

Spacecraft's relative velocity to Deimos will be quite high at the closest distance, as shown above. The challenge is that Deimos-centric pointing will not be maintained for several minutes before and after the closest approach, because the required angular rate of the along-track direction would exceed the capability of the spacecraft. For the case of the closest distance around 300 km, we represent the evolution of MIRS resolution as a function of time for the 3:5 and the 1:1 resonance flyby trajectory in Fig. 20. At 300 km distance, MIRS can achieve 100 m resolution, however, as stated above, Deimos-centric pointing will not be maintained several minutes before and after closest approach, the actual best achievable resolution will be worse. If we consider the time during which distance will

be close enough to have 500 m resolution, it varies from 2 h for the 3:5 trajectory down to 54 min for the 1:1 trajectory (Fig. 20). Note that time during which Deimos-centric pointing will not be maintained has to be subtracted to get the actual observation time.

MSA

The situation is the same for the MSA in the Deimos flyby observation as in the nominal Phobos observation. The solar wind will be continuously observed by the MSA, while those scattered at the Deimos surface are measurable only in the neighboring dayside of Deimos. The requirements to observe secondary ions sputtered from Deimos are that the spacecraft is around the terminator, and that solar wind electric field (E) directs from Deimos to the spacecraft. Smaller distance between the spacecraft and Deimos effectively increases the observation opportunity. When the spacecraft is downstream of Deimos against the solar wind, the MSA may observe secondary ions from Deimos, which are in the pickup motions by the solar wind (e.g., Halekas et al. 2013).

Nakamura *et al. Earth, Planets and Space*   (2021) 73:227

Page 25 of 27

MEGANE

The neutron spectrometer portion of MEGANE has the potential to acquire measurements during the Deimos flybys phase, but whether such measurements are possible depends strongly on the flyby altitude as well as the number of flybys and the speeds. For example, five flybys of Deimos at 1 km/s with a 10-km closest-approach altitude has been modeled to provide compositional information about Deimos by the MEGANE neutron spectrometer that could be compared to Phobos (Lawrence et al. 2019). A comparison of the same neutron spectrometer measurement for Phobos and Deimos by MEGANE would enable important insight into the fundamental nature of the two Martian moons and in particular help address the basic question about whether the two moons are compositionally the same or different. Thus, while Deimos measurements by MEGANE would be challenging, this comparison of the two moons by the exact same measurement is highly compelling scientifically. If after a few successful Deimos flybys, the close-approach altitude of the spacecraft can be lowered, it is possible that MEGANE can make this key measurement.

CMDM

The spacecraft will remain at the orbit on the Mars' equatorial plane during most of its stay around Mars. According to Krivov and Hamilton (1997), during this period of observation, it is difficult to determine the thickness of the dust ring structure because the MMX spacecraft never goes outside the Phobos ring, which is thought to be about 170 km thick. However, the spacecraft will pass through the outer edge of the Phobos dust ring on the orbit from the Phobos orbit to the transfer orbit to the flyby orbit to Deimos, which has a slightly larger orbital inclination than Phobos. At that orbit, the CMDM in-situ observations will determine the outer edge of the Phobos dust ring structure.

On the other hand, in the dust measurement during the Deimos flyby in Phase 5, the CMDM may detect only the dust particles ejected from Deimos. The apocentre of the Phobos dust ring does not reach the Deimos orbit even if the eccentricity changes (Krivov and Hamilton 1997; Liu and Schmidt 2020). On the other hand, dust particles from Deimos can be observed at the position of Phobos orbit because the pericenter point becomes closer to Mars due to perturbation by solar radiation, and it may be difficult to distinguish those two different origin dust particles. If we know the net flux of Deimos-origin particles in Deimos orbit, we may be able to estimate the net flux of Phobos-origin particles within the dust flux in Phobos orbit.

While Phobos-origin dust remains in orbit for only less than a 100 years, Deimos-origin dust remains in orbit for more than 10,000 years, so the total number of dust particles in the entire torus is larger for Deimos (Krivov and Hamilton 1997; Liu and Schmidt 2020). However, particles of Deimos origin form a torus, and the structure of the Deimos torus is probably considerably larger than that of the Phobos ring. Depending on how the Deimos torus extends, the number density of dust in the Deimos torus could be smaller than in the Phobos dust ring.

Conclusions

A detailed scientific observation plan was developed for Phobos from various QSOs with different altitudes. The observation plan became complex, as various factors, such as solar conjunctions, eclipses and occultations by Mars and Phobos, had to be taken into account. The observation period will be long enough to stay around Phobos for 2.5 years, but the actual observation period will be shorter due to the effects of conjunctions and eclipses. Within these limitations, we have developed an observational plan for Phobos that is sufficient to fulfill the scientific objectives of the MMX mission. On the other hand, we are still in the process of developing a detailed observation plan for Deimos. The general plan is to insert the spacecraft into two resonant orbits and conduct a number of flyby to observe as much of the Deimos surface as possible.

Nakamura *et al. Earth, Planets and Space*   (2021) 73:227

Page 26 of 27

Author details

[1]Tohoku University, Sendai, Japan. [2]RDD (Research and Development Directorate)/JAXA, Sagamihara/Tsukuba, Japan. [3]NIAIST, Tokyo, Japan. [4]QST, Chiba, Japan. [5]Chiba Institute of Technology, Narashino, Japan. [6]Rikkyo University, Tokyo, Japan. [7]National Astronomical Observatory of Japan, Oshu, Japan. [8]The Graduate University for Advanced Studies, SOKENDAI, Hayama, Japan. [9]ISAS/JAXA, Sagamihara, Japan. [10]University of Surrey, Guildford, UK. [11]Johns Hopkins University, Applied Physics Laboratory, Laurel, USA. [12]LESIA-Observatoire de Paris, Université PSL, CNRS, Sorbonne Université, Université de Paris, Paris, France. [13]CNES, Toulouse, France. [14]Osaka University, Toyonaka, Japan. [15]Deutsches Zentrum für Luft- und Raumfahrt, DLR, Cologne, Germany. [16]Université Côte d'Azur, Observatoire de la Côte d'Azur, CNRS, Laboratoire Lagrange, Nice, France. [17]Aizu University, Aizuwakamatsu, Japan. [18]The University of Tokyo, Tokyo, Japan. [19]JAXA Space Exploration Center (JSEC)/JAXA, Tokyo, Japan. [20]Mitsubishi Electric, Tokyo, Japan. [21]NHK, Tokyo, Japan. [22]JAMSS, Tsukuba, Japan. [23]Hokkaido University, Sapporo, Japan.

References

Baresi N, Dei Tos DA, Ikeda H, Kawakatsu Y (2020) Trajectory design and maintenance of the Martian Moons eXploration mission around phobos. J Guid Control Dyn 44:1–12. https://doi.org/10.2514/1.G005041

Barruci MA et al (2021) MIRS an Imaging spectrometer for the MMX mission. Earth Planets Space. https://doi.org/10.1186/s40623-021-01423-2

Basilevsky AT et al (2014) The surface geology and geomorphology of Phobos. Planet Space Sci 102:95–118. https://doi.org/10.1016/j.pss.2014.04.013

Burns JA (1978) The dynamical evolution and origin of the martian moons. Vistas Astron 22:19–210. https://doi.org/10.1016/0083-6656(78)90015-6

Chabot NL et al (2021) MEGANE investigations of Phobos and the small body mapping tool. Earth Planets Space. https://doi.org/10.1186/s40623-021-01509-x

Chikazawa T, Baresi N, Campagnola S, Ozaki N, Kawakatsu Y (2021) Minimizing eclipses via synodic resonant orbits with applications to EQUULEUS and MMX. Acta Astronaut 180:679–692. https://doi.org/10.1016/j.actaastro.2020.12.028

Cho Y et al (2021) In-situ science on Phobos with the Raman spectrometer for MMX (RAX): preliminary design and feasibility of Raman measurements. Earth Planets Space. https://doi.org/10.1186/s40623-021-01496-z

Craddock RA (2011) Are Phobos and Deimos the result of a giant impact? Icarus 211:1150–1161. https://doi.org/10.1016/j.icarus.2010.10.023

Duxbury TC, Zakharov AV, Hoffmann H, Guinness EA (2014a) Spacecraft exploration of Phobos and Deimos. Planet Space Sci 102:9–17. https://doi.org/10.1016/j.pss.2013.12.008

Elphic RC, Funsten HO III, Barraclough BL, McComas DJ, Paffett MT, Vaniman DT, Heiken G (1991) Lunar surface composition and solar wind-induced secondary ion mass spectrometry. Geophys Res Lett 18(11):2165–2168. https://doi.org/10.1029/91GL02669

Ernst CM, Daly RT, Gaskell RW, Barnouin OS, Nair H, Hyatt BA, Al Asad MM, Wilcomb KK (2021) High-resolution shape models of Phobos and Deimos from stereophotoclinometry. Earth Planets Space. https://doi.org/10.21203/rs.3.rs-414828/v1

Fujiwara A, Kawaguchi J, Yeomans DK, Abe M, Mukai T, Okada T, Saito J, Yano H, Yoshikawa M, Scheeres DJ, Barnouin-Jha O, Cheng AF, Demura H, Gaskell RW, Hirata N, Ikeda H, Kominato T, Miyamoto H, Nakamura AM, Nakamura R, Sasaki S, Uesugi K (2006) The rubble-pile asteroid Itokawa as observed by Hayabusa. Science 312(5778):1330–1334. https://doi.org/10.1126/science.1125841

Halekas JS, Poppe AR, Delory GT, Sarantos M, McFadden JP (2013) Using ARTEMIS pickup ion observations to place constraints on the lunar atmosphere. J Geophys Res Planets 118(1):81–88. https://doi.org/10.1029/2012JE004292

Hamilton DP (1996) The asymmetric time-variable rings of Mars. Icarus 119:153–172. https://doi.org/10.1006/icar.1996.0008

Hirata N, Namiki N, Yoshida F, Matsumoto K, Noda H, Senshu H, Mizuno T, Terui F, Ishihara Y, Yamada R, Yamamoto K, Abe S, Noguchi R, Hirata N, Tsuda Y (2021) Rotational effect as the possible cause of the east–west asymmetric crater rims on Ryugu observed by LIDAR data. Icarus 354:114073. https://doi.org/10.1016/j.icarus.2020.114073

Ho TM, Jaumann R, Bibring JP, Grott M, Glaßmeier KH, Moussi A, Krause C, Auster U, Baturkin V, Biele J, Cordero F, Cozzoni B, Dudal C, Fantinati C, Grimm C, Grundmann JT, Hamm M, Hercik D, Kayal K, Knollenberg J, Küchemann O, Ksenik E, Lange C, Lange M, Lorda L, Maibaum M, Mimasu Y, Cenac-Morthe C, Okada T, Otto K, Pilorget C, Reill J, Saiki T, Sasaki K, Schlotterer M, Schmitz N, Schröder S, Termtanasombat N, Toth N, Tsuda Y, Ulamec S, Wolff F, Yoshimitsu T, Ziach C (2021) The MASCOT lander aboard Hayabusa2: the in-situ exploration of NEA (162173) Ryugu. Planet Space Sci 200:105200. https://doi.org/10.1016/j.pss.2021.105200

Horányi M, Szalay JR, Kempf S, Schmidt J, Grün E, Srama R, Sternovsky Z (2015) A permanent, asymmetric dust cloud around the Moon. Nature 522:324–326. https://doi.org/10.1038/nature14479

Ishimoto H (1996) Formation of Phobos/Deimos dust rings. Icarus 122:153–165. https://doi.org/10.1006/icar.1996.0116

Jaumann R, Schmitz N, Ho TM, Schröder SE, Otto KA, Stephan K, Elgner S, Krohn K, Preusker F, Scholten F, Biele J, Ulamec S, Krause C, Sugita S, Matz KD, Roatsch T, Parekh R, Mottola S, Grott M, Michel P, Trauthan F, Koncz A, Michaelis H, Lange C, Grundmann JT, Maibaum M, Sasaki K, Wolff F, Reill J, Moussi-Soffys A, Lorda L, Neumann W, Vincent JB, Wagner R, Bibring JP, Kameda S, Yano H, Watanabe S, Yoshikawa M, Tsuda Y, Okada T, Yoshimitsu T, Mimasu Y, Saiki T, Yabuta H, Rauer H, Honda R, Morota T, Yokota Y, Kouyama T (2019) Images from the surface of asteroid Ryugu show rocks similar to carbonaceous chondrite meteorites. Science 365:817–820. https://doi.org/10.1126/science.aaw8627

Kameda S et al (2021) Design of telescopic nadir imager for geomorphology (TENGOO) and observation of surface reflectance by optical chromatic imager (OROCHI) for the Martian Moons Exploration (MMX). Earth Planets Space. https://doi.org/10.1186/s40623-021-01462-9

Kobayashi M, Krüger H, Senshu H, Wada K, Okudaira O, Sasaki S, Kimura H (2018) In situ observations of dust particles in Martian dust belts using a large-sensitive-area dust sensor. Planet Space Sci 156:41–46. https://doi.org/10.1016/j.pss.2017.12.011

Krivov AV, Hamilton DP (1997) Martian dust belts: waiting for discovery. Icarus 128:335–353. https://doi.org/10.1006/icar.1997.5753

Krüger H, Krivov A, Hamilton D, Grün E (1999) Detection of an impact-generated dust cloud around Ganymede. Nature 399:558–560. https://doi.org/10.1038/21136

Kuramoto K et al (2021) Martian moons exploration MMX: sample return mission to Phobos elucidating formation processes of habitable planets. Earth Planets Space. https://doi.org/10.1186/s40623-021-01545-7

Lawrence DJ, Peplowski PN, Beck AW, Burks MT, Chabot NL, Cully MJ, Elphic RC, Ernst CM, Fix S, Goldsten JO, Hoffer EM, Kusano H, Murchie SL, Schratz BC, Usui T, Yokley ZW (2019) Measuring the elemental composition of Phobos: the Mars-moon exploration with gamma rays and neutrons (MEGANE) investigation for the Martian Moons eXploration (MMX) mission. Earth Space Sci 6:2605–2623. https://doi.org/10.1029/2019EA000811

Liu X, Schmidt J (2020) Configuration of the Martian dust rings: shapes, densities, and size distributions from direct integrations of particle trajectories. Mon Not R Astron Soc 500(3):2979–2985. https://doi.org/10.1093/mnras/staa3084

Marov MY, Avduevsky VS, Akim EL, Eneev TM, Kremnev RS, Kulikov SD, Pichkhadze KM, Popov GA, Rogovsky GN (2004) Phobos-Grunt: Russian sample return mission. Adv Space Res 33:2276–2280. https://doi.org/10.1016/S0273-1177(03)00515-5

Matsumoto K et al (2021) MMX geodesy investigations: science requirements and observation strategy. Earth Planets Space. https://doi.org/10.1186/s40623-021-01500-6

Michel P et al (2021) The MMX rover: performing in-situ surface investigations on Phobos. Earth Planets Space. https://doi.org/10.1186/s40623-021-01464-7

Nakamura *et al. Earth, Planets and Space*   (2021) 73:227

Page 27 of 27

Nakamura T, Noguchi T, Tanaka M, Zolensky ME, Kimura M, Tsuchiyama A, Nakato A, Ogami T, Ishida H, Uesugi M, Yada T, Shirai K, Fujimura A, Okazaki R, Sandford SA, Ishibashi Y, Abe M, Okada T, Ueno M, Mukai T, Yoshikawa M, Kawaguchi J (2011) Itokawa dust particles: a direct link between S-type asteroids and ordinary chondrites. Science 333:1113–1116. https://doi.org/10.1126/science.1207758

Nishino MN, Fujimoto M, Saito Y, Yokota S, Kasahara Y, Omura Y, Goto Y, Hashimoto K, Kumamoto A, Ono T, Tsunakawa H, Matsushima M, Takahashi F, Shibuya H, Shimizu H, Terasawa T (2010) Effect of the solar wind proton entry into the deepest lunar wake. Geophys Res Lett 37:L12106. https://doi.org/10.1029/2010GL043948

Ogohara K et al (2021) The Mars system revealed by the Martian Moons eXploration mission. Earth Planets Space. https://doi.org/10.1186/s40623-021-01417-0

Peplowski PN (2016) The global elemental composition of 433 Eros: first results from the NEAR gamma-ray spectrometer orbital dataset. Planet Space Sci 134:36–51. https://doi.org/10.1016/j.pss.2016.10.006

Pushparaj N, Baresi N, Ichinomiya K, Kawakatsu Y (2021) Transfers around Phobos via bifurcated retrograde orbits: applications to Martian Moons eXploration mission. Acta Astronaut 181:70–80. https://doi.org/10.1016/j.actaastro.2021.01.016

Rosenblatt P (2011) The origin of the Martian moons revisited. Astron Astrophys Rev 19:44. https://doi.org/10.1007/s00159-011-0044-6

Sagdeev R, Zakharov A (1989) Brief history of the Phobos mission. Nature 341:581–585. https://doi.org/10.1038/341581a0

Saito Y, Yokota S, Tanaka T, Asamura K, Nishino MN, Fujimoto M, Tsunakawa H, Shibuya H, Matsushima M, Shimizu H, Takahashi F, Mukai T, Terasawa T (2008) Solar wind proton reflection at the lunar surface: low energy ion measurement by MAP-PACE onboard SELENE (KAGUYA). Geophys Res Lett 35:L24205. https://doi.org/10.1029/2008GL036077

Saito Y, Nishino MN, Fujimoto M, Yamamoto T, Yokota S, Tsunakawa H, Shibuya S, Matsushima M, Shimizu H, Takahashi F (2012) Simultaneous observation of the electron acceleration and ion deceleration over lunar magnetic anomalies. Earth Planets Space 64(2):83–92. https://doi.org/10.5047/eps.2011.07.011

Sasaki S (1999) Dust ring/torus around Mars, waiting for detection by NOZOMI. Adv Space Res 23:1907–1910. https://doi.org/10.1016/S0273-1177(99)00278-1

Schaible MJ, Dukes CA, Hutcherson AC, Lee P, Collier MR, Johnson RE (2017) Solar wind sputtering rates of small bodies and ion mass spectrometry detection of secondary ions. J Geophys Res Planets 122:1968–1983. https://doi.org/10.1002/2017JE005359

Senshu H et al (2021) Light detection and ranging (LIDAR) laser altimeter for the Martian Moons Exploration (MMX) spacecraft. Earth Planets Space. https://doi.org/10.1186/s40623-021-01537-7

Stubbs TJ, Farrell WM, Halekas JS, Burchill JK, Collier MR, Zimmerman MI, Vondrak RR, Delory GT, Pfaff RF (2014) Dependence of lunar surface charging on solar wind plasma conditions and solar irradiation. Planet Space Sci 90:10–27. https://doi.org/10.1016/j.pss.2013.07.008

Tsunakawa H, Takahashi F, Shimizu H, Shibuya H, Matsushima M (2015) Surface vector mapping of magnetic anomalies over the Moon using Kaguya and lunar prospector observations. J Geophys Res 120:1160–1185. https://doi.org/10.1002/2014JE004785

Ulamec S, Michel P, Grott M, Böttger U, Hübers HW, Murdoch N, Vernazza P, Özgür K, Knollenberg J, Willner K, Grebenstein M, Mary S, Chazalnoel P, Biele J, Krause C, Ho TM, Lange C, Grundmann JT, Sasaki K, Maibaum M, Küchemann O, Reill J, Chalon M, Barthelmes S, Lichtenheldt R, Krenn R, Smisek M, Bertrand J, Moussi A, Delmas C, Tardivel S, Arrat D, IJpelaan F, Melac L, Lorda L, Remetean E, Lange M, Mierheim O, Reershemius S, Usui T, Matsuoko M, Nakamura T, Wada K, Miyamoto H, Kuramoto K, LeMaitre Julia, Mas G, Delpech M, Celine L, Rafflegeau A, Boirad H, Schmisser R, Virmontois C, Cenac-Morthe C, Besson A, Rull F (2019) A rover for the JAXA MMX Mission to Phobos. In: 70th international astronautical congress, Washington D.C., USA, 19–25 October 2019

Watanabe S, Hirabayashi M, Hirata N, Hirata N, Noguchi R, Shimaki Y, Ikeda H, Tatsumi E, Yoshikawa M, KikuchiS YH, Nakamura T, Tachibana S, Ishihara Y, Morota T, Kitazato K, Sakatani N, Matsumoto K, Wada K, Senshu T, Honda C, Michikami T, Takeuchi H, Kouyama T, Honda R, Kameda S, Fuse T, Miyamoto H, Komatsu G, Sugita S, Okada T, Namiki N, Arakawa M, Ishiguro M, Abe M, Gaskell R, Palmer E, Barnouin OS, Michel P, French AS, McMahon JW, Scheeres DJ, Abell PA, Yamamoto Y, Tanaka S, Shirai K, Matsuoka M,

Yamada M, Yokota Y, Suzuki H, Yoshioka K, Cho Y, Tanaka S, Nishikawa N, Sugiyama T, Kikuchi H, Hemmi R, Yamaguchi T, Ogawa N, Ono G, Mimasu Y, Yoshikawa K, Takahashi T, Takei Y, Fujii A, Hirose C, Iwata T, Hayakawa M, Hosoda S, Mori O, Sawada H, Shimada T, Soldini S, Yano H, Tsukizaki R, Ozaki M, Iijima Y, Ogawa K, Fujimoto M, Ho TM, Moussi A, Jaumann R, Bibring JP, Krause C, Terui F, Saiki T, Nakazawa S, Tsuda Y (2019) Hayabusa2 arrives at the carbonaceous asteroid 162173 Ryugu—a spinning top-shaped rubble pile. Science 364:268–272. https://doi.org/10.1126/science.aav8032

Witasse O, Duxbury T, Chicarro A, Altobelli N, Andert T, Aronica A, Barabash S, Bertaux JL, Bibring JP, Cardesin-Moinelo A, Cichetti A, Companys V, Dehant V, Denis M, Formisano V, Futaana Y, Giuranna M, Gondet B, Heather D, HoffmannH HM, Manaud N, Martin P, Matz KD, Montmessin F, Morley T, Mueller M, Neukum G, Oberst J, Orosei R, Pätzold M, Picardi G, Pischel R, Plaut JJ, Reberac A, Voss PP, Roatsch T, Rosenblatt P, Remus S, Schmedemann N, Willner K, Zegers T (2014) Mars express investigations of Phobos and Deimos. Planet Space Sci 102:18–34. https://doi.org/10.1016/j.pss.2013.08.002

Yokota S, Saito Y (2005) Estimation of picked-up lunar ions for future compositional remote SIMS analyses of the lunar surface. Earth Planets Space 57:281–289. https://doi.org/10.1186/BF03352564

Yokota S et al (2021) In situ observations of ions and magnetic field around Phobos: the mass spectrum analyzer (MSA) for the Martian Moons eXploration (MMX) mission. Earth Planets Space. https://doi.org/10.1186/s40623-021-01452-x

Publisher's Note